LUND UNIVERSITY

FACULTY OF ENGINEERING

DIVISION OF SOLID STATE PHYSICS

µLEDs for optogenetics

A Master's Thesis in Physics

Lukas Wendt

Supervised by

Olof Hultin

October 2018

Abstract

Optogenetics is unfolding new ways for us to study the nervous system and could one day be a standard approach to treat neurological diseases like epilepsy. To selectively study the effects on a subcellular level, microscopic light sources are needed. Nanostructure, light-emitting diodes (LEDs) can realize this criteria but processing to connect and protect them is necessary before any fruitful optogenetic tests can be conducted. In this work, micron sized, III-nitride, LED light sources were created using microfabrication techniques such as lithography, etching and thin film deposition. Experimental biointegration and passivation schemes were then used to build a prototype optogenetic device for stimulation of primary neurons grown *in vitro* onto the device, in close proximity to the light emitters. Favorable electrical and optical characteristics were obtained for the individual nanostructure LEDs, lighting up brightly at a wavelength around 470 nm. However, larger devices revealed process related and uniformity challenges to overcome. Additionally, the biointegration design would prove too complex and in need of further improvement. This effort, while not outputting a fully functioning device, has contributed to development of the utilized nanostructure LED technology so that we may see more of it in the future.

Svensk sammanfattning

Optogenetik är en teknik som öppnar upp för nya sätt att studera vårt nervsystem och kan en dag leda till behandlingsmetoder för neurologiska sjukdomar såsom epilepsi. För att selektivt studera effekterna på en subcellulär nivå behövs mikroskopiska ljuskällor. Nanostrukturbaserade lysdioder kan realisera detta, men processning för att ansluta och skydda dem är nödvändigt innan fruktbara optogenetiska tester kan genomföras. I detta arbete har mikrometerstora III-nitrid lysdioder utvecklats med hjälp av bland annat litografi, etsning och tunnfilmstekniker. Experimentella metoder för biointegrering och passivering användes därefter för att skapa en optogenetisk prototyp i syfte att kunna stimulera primära nervceller odlade *in vitro* på enheten, i nära anslutning till ljuskällorna. Gynnsamma elektriska och optiska egenskaper erhölls för enskilda lysdioder, som emitterade tydligt med våglängden 470 nm. Större enheter visade emellertid att process- och uniformitetsrelaterade utmaningar återstår att adressera. Utöver detta visade sig biointegreringsdesignen vara för komplex och i behov av ytterligare iterationer. Trots att arbetet inte levererat en fullt funktionell lösning har våra ansträngningar bidragit till att utveckla den specifika lysiodstekniken så att vi kan få se mer av den i fortsättningen.

Contents

Abstract **1**

Svensk sammanfattning **2**

Contents **3**

Abbreviations **4**

1 Introduction **6**

2 Theory **7**
2.1 Light-emitting diodes . . . 7
2.1.1 The p-n junction . . . 8
2.1.2 Recombination and emission . . . 9
2.1.3 Quantum wells and heterostructures . . . 10
2.1.4 The nitride material system . . . 11
2.1.5 Platelets . . . 13
2.2 Optogenetics . . . 14
2.2.1 Neurons and action potentials . . . 15
2.2.2 Epilepsy . . . 16
2.2.3 Patch-clamp technique . . . 16

3 Methodology **17**
3.1 Platelet synthesis . . . 17
3.2 LED processing . . . 19
3.2.1 Rapid thermal annealing . . . 19
3.2.2 Atomic layer deposition . . . 20
3.2.3 Spacer layers . . . 20
3.2.4 Etch hole definition . . . 22
3.2.5 Contact definition . . . 23
3.3 Characterization . . . 25
3.4 Packaging . . . 27

4 Results **28**
4.1 Current-voltage characteristics . . . 29
4.2 Electroluminescence . . . 33
4.3 Biointegration . . . 35

5 Discussion **37**
5.1 Prototype evaluation 37
5.2 Future prospects 38
5.3 Ethics, risks and sustainability 40

6 Conclusion **41**

Acknowledgments **42**

References **43**

Abbreviations

AlGaN Aluminium gallium nitride

Al_2O_3 Aluminium oxide

AlN Aluminium nitride

aCSF Artificial cerebrospinal fluid

ALD Atomic layer deposition

BOE Buffered oxide etch

ChR2 Channelrhodopsin-2

I-V Current-voltage

DIW Deionized water

DC Direct current

EL Electroluminescence

EBL Electron beam lithography

EEG Experimental Epilepsy Group

EQE External quantum efficiency

FWHM Full width half maximum

GaN Gallium nitride

InGaN Indium gallium nitride

InN Indium nitride

IPA Isopropanol

LED	Light-emitting diode
LPCVD	Low pressure chemical vapor deposition
LNL	Lund Nano Lab
MOVPE	Metalorganic vapor phase epitaxy
MIBK	Methyl isobutyl ketone
µLED	Micrometer-scale light-emitting diode
NW	Nanowire
OLED	Organic light-emitting diode
PMMA	Poly(methyl methacrylate)
QCSE	Quantum-confined Stark effect
QW	Quantum well
RIE	Reactive ion etching
RGB	Red green blue
α-Al_2O_3	Sapphire
SEM	Scanning electron microscopy
SAG	Selective area growth
Si_3N_4	Silicon nitride
SMU	Source measure unit
TD	Threading dislocation
TEGa	Triethylgallium
UV	Ultraviolet
WF	Write field

Chapter 1

Introduction

Optogenetics, the act of controlling biological activity by optical stimulation, is developing into an important tool for understanding our complex nervous system. It also carries the potential to be utilized for treating various neurological diseases such as epilepsy. However, to study its effects better and more locally, miniaturized, close proximity photon sources are needed. Until recently light sources used in optogenetics have been large and excessively luminous, effectively stimulating a lot more than the intended biological components. Even now, as much effort is being put into creating more competent devices [1–8], the smallest tested emitters, $6 \times 9\,\mu m$ large [7], are not yet enough to selectively stimulate the smallest cell features, such as an individual synapse.

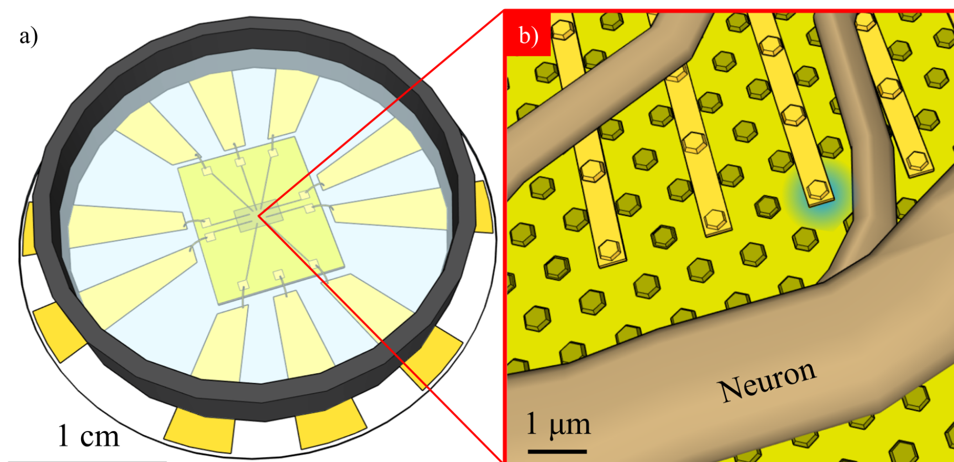

Figure 1.1: **a)** Model showing a passivated device chip mounted on a glass disk with deposited metal fields, a 3D printed pool rim and wire bonds submerged in extracellular media. **b)** Zoomed in view of a single µLED illuminating a nearby neuron from underneath its contact.

The aim of this project has been to develop and test a high resolution optogenetic tool for controlling neurons to study neurological disorders on the subcellular level. By creating a robust and capable device with multiple micrometer-scale LEDs (µLEDs) we had high hopes to measure

neural response to very localized blue light stimulus on transgenic mouse primary cells, cultured from a subject animal directly onto the LED chip, as illustrated by figure 1.1. As a side effect, we also wanted to accumulate some practical experience of bio-integrating these miniature optoelectronic devices for future research and projects, similar in nature.

I write this thesis for my Master of Science degree in engineering nanoscience at the Lund University Faculty of Engineering. The project was setup as a collaboration between the Division of Solid State Physics, nitride group and the Department of Clinical Sciences, Experimental Epilepsy Group (EEG) where Daniel Jaghobi has been writing a separate thesis on the biological testing of our LED devices supervised by Jenny Wickham and Mérab Kokaia.

The report will focus on the creation of µLED devices for use in medical science, so the theoretical background of these light sources will be covered as well as an introduction to optogenetics. This will be followed by a walk-through of the processing steps performed in Lund Nano Lab (LNL) to create the devices and results from characterization and testing. Finally, we will discuss our findings and future implications.

Chapter 2

Theory

In this chapter the theory of solid state LEDs will be explained from a basic semiconductor physics level as well as the specifics of III-nitride materials and nanostructure techniques to improve their performance. Short summaries of optogenetics, epilepsy, neurons and electrophysiologic techniques will then follow to acquaint the reader to these subjects.

2.1 Light-emitting diodes

LEDs are revolutionizing how we light up our world [9–11]. They work by the physical phenomenon electroluminescence (EL), converting electrical currents to light through the process of electron and hole recombination. Apart from the standard solid state semiconductor LED, a variety of different ways to achieve EL exist such as the organic LED (OLED). As the main subject of this thesis is the processing, characterization and packaging of periodic table group III-V compound devices, the following sections will focus on how inorganic, semiconductor LEDs operate.

2.1.1 The p-n junction

A p-n junction is created between two regions of a semiconductor material, doped with atomic impurities. One of these regions being p-type, with electron acceptor atoms and the other being n-type, with electron donor atoms. When brought together, holes and electrons will diffuse over the junction, creating a charged depletion region at the interface as donor and acceptor impurities are ionized. The ionized dopant atoms cause an electric field and a potential difference V_{bi} over the depletion region width w, in accordance to equations 2.1 and 2.2.

$$V_{bi} = \frac{kT}{e} \ln \frac{N_A N_D}{{n_i}^2} \tag{2.1}$$

$$w = \sqrt{\frac{2\epsilon_0\epsilon_r}{e}(V_{bi} - V)\left(\frac{1}{N_A} + \frac{1}{N_D}\right)} \tag{2.2}$$

where k is the Boltzmann constant, T is the temperature, e is the elementary charge, $N_{D,A}$ are n-type donor and p-type acceptor atom concentrations, n_i is the intrinsic carrier concentration, $\epsilon_{0,r}$ are the vacuum and semiconductor relative permittivities respectively and V is the applied voltage bias.

The potential V_{bi} corresponds to the bending of energy bands at thermal equilibrium, as seen in figure 2.1. Free electrons and holes, also called charge carriers, are found above the n-type conduction band edge energy E_C and below the p-type valence band edge energy E_V respectively while the Fermi level E_F, is flat across the junction. By applying a forward bias over the p-n junction, the potential barrier can be lowered. What ensues is that currents of electrons and holes passing over the depletion region increase exponentially, due to the free carrier distribution inside the bands. This is the principle behind the current-rectifying diode, where the current-voltage (I-V) relationship is described by equations 2.3 and 2.4, evolved from the Shockley diode equation [12].

$$I = I_s(\exp\left(\frac{eV}{\eta kT}\right) - 1) \tag{2.3}$$

$$I_s = eA\left(\sqrt{\frac{D_p}{\tau_p}}\frac{{n_i}^2}{N_D} + \sqrt{\frac{D_n}{\tau_n}}\frac{{n_i}^2}{N_A}\right) \tag{2.4}$$

where I is the current, I_s is the reverse bias saturation current, η is the ideality factor, A is the junction area, $D_{p,n}$ are hole and electron diffusion constants and $\tau_{p,n}$ are hole and electron charge carrier lifetimes.

Not included in this model however is the reverse current breakdown, which can occur either because of avalanche multiplication or Zener tunneling of majority carriers over the junction into the opposite band, if the diode is highly doped. Figure 2.1 illustrates p-n function and how the band diagram relates to its I-V characteristics.

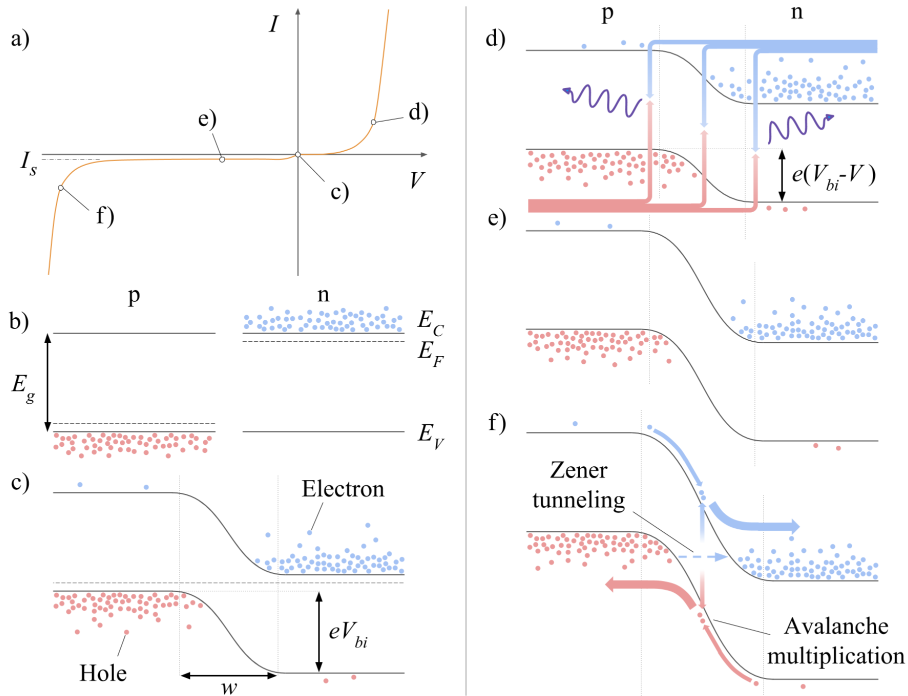

Figure 2.1: **a)** Diode I-V characteristics. **b)** Separate p and n-doped semiconductor band diagrams. **c)** p-n junction at equilibrium. **d)** Forward bias with recombination currents and photon emission. **e)** Reverse bias. **f)** Reverse bias breakdown with Zener and avalanche currents. Electron and hole concentrations serve only to visualize p-n operation.

2.1.2 Recombination and emission

As they travel across the depletion region in larger numbers, free electrons and holes end up in the same spatial volume of material as their majority carrier counterparts. This leads to an increase in the rate R at which they can recombine, as indicated by equation 2.5, the bimolecular recombination equation.

$$R = Bnp \tag{2.5}$$

where B is the bimolecular recombination coefficient and n, p are the local electron and hole concentrations respectively.

When an electron and a hole recombine, emission of a photon may occur. The energy it receives is decided by how much energy the electron loses during recombination. This facilitates a peak in emission energy slightly above the band gap energy E_g due to the combination of the density of states and the Boltzmann distribution [13]. Equation 2.6 shows the relationship between band gap and peak photon wavelength λ.

$$E_g = E_C - E_V \approx h\nu = \frac{hc}{\lambda} \tag{2.6}$$

where h is the Planck constant, ν is the peak photon frequency and c is the speed of light.

For LEDs radiative recombination, creating photons, is the preferred alternative to non-radiative recombination, when the electron energy is converted to a phonon or lattice vibrations and eventually heat. There are several different causes for non-radiative recombination. Shockley-Read-Hall, or deep level trap recombination describes electrons recombining via inhabitable energy states inside the band gap. Auger recombination is another form of non-radiative recombination where the energy lost by the recombining electron is dissipated by exciting another electron far into the conduction band instead of emitting a photon. The regular bulk band diagram relies on crystal periodicity and could therefore be unpredictable near surfaces and edges. Surface recombination can occur due to dangling bonds and local surface reconstruction of the atomic structure differing from that in the bulk. Potentially these effects will lead to unintended energy states and recombination routes.

Direct band gap semiconductors can transfer most of the recombination energy to the photons while an indirect band gap means some energy will be lost to phonons, reducing the light emission efficiency. The external quantum efficiency EQE from equation 2.7 is a common gauge for LED efficiency, comparing the ratio between photons escaping to free space surrounding the semiconductor die and injected electrons [13].

$$\text{EQE} = \frac{\text{photons emitted}}{\text{electrons injected}} = \frac{P/(h\nu)}{I/e} \tag{2.7}$$

where P is the total emitted photon power from the LED into free space.

2.1.3 Quantum wells and heterostructures

A quantum well (QW) is an ultra thin layer of lower E_g, semiconductor material often used in LEDs to increase the radiative recombination rate and emission efficiency. The well layer is typically only a few nanometers long and sandwiched between the p and n-doped regions. Here it can catch and concentrate a large portion of charge carriers into a very small volume where recombination will occur more frequently due to the larger p and n concentration overlap. QW emission energy can be tuned by altering the effective band gap with material composition and to some extent quantum confinement. By making the layer thinner, the lowest possible carrier states, get squeezed further into the band causing the expected emission peak to be shifted to higher energies.

Modern LEDs often feature multiple quantum wells placed in series inside a so-called active region confined by regions of higher band gap material. A p-doped, higher E_g, electron blocking layer at the transition from the active region to the p-side, is another common type of heterostructure, preventing electrons from crossing into the p-side, as their mobility is typically considerably higher than that of holes. While

heterostructures are very useful for many types of LED devices there are some associated problems with band barriers being formed at the interface from charge carriers diffusing over it, creating an electric field, similarly to the mechanism of the depletion region formation in the basic p-n junction. These heterostructure barrier effects can be mitigated by grading the material compositions close to the interface to better match that of the other material but at the cost of extra process complexity [13].

2.1.4 The nitride material system

Gallium nitride (GaN) together with indium nitride (InN) and aluminium nitride (AlN) constitute the basis for the III-nitride subgroup of the III-V compound semiconductors. These direct band gap semiconductors have played an echoing part in the development of efficient, high brightness LEDs ever since the efforts of Shuji Nakamura, Hiroshi Amano and Isamu Akasaki *et al.* in the late 1980s and early 1990s which earned them the Nobel Prize in Physics 2014. Their contributions include improving GaN crystal quality [14], developing ways to activate the p-type doping [15–18] and demonstration of the first high luminance blue LEDs [19, 20]. Blue GaN LEDs based on Mg acceptor and Si donor dopant atoms with indium gallium nitride (InGaN) QWs, as the one sketched in figure 2.2, have become more efficient since then, achieving impressive values for EQE in excess of 84 % [21]. Because of this trend, they have been widely adopted for general lighting by using phosphor coating modulation techniques to create a more continuous spectrum of white light [22].

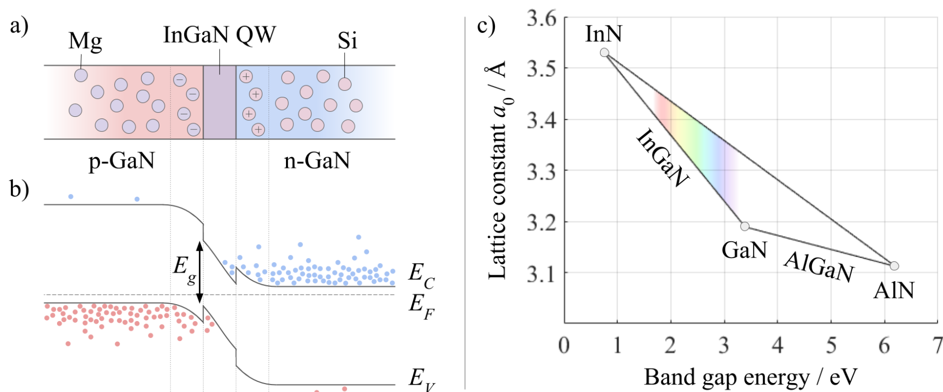

Figure 2.2: **a)** GaN/InGaN LED schematic with Mg acceptors and Si donors ionized in the depletion region. **b)** Not to scale, energy band diagram for the same structure at thermal equilibrium. **c)** Lattice constant vs E_g graph for the III-nitrdes at 300 K, using data from table 2.1, illustrating how varying Ga/In/Al ratios can be used to tune photon emission energy. Graph is idealized by neglecting curve bowing.

The band gap of the InGaN QW can be engineered by varying the Ga/In ratio, to create photons of any colour you like, from 0.72 eV

(1 722 nm) to 3.39 eV (366 nm), also manifested in figure 2.2. GaN and even some InGaN compositions will emit in the ultraviolet (UV) spectrum with aluminium gallium nitride (AlGaN) enabling emission in the deep UV range [23]. Doped AlGaN layers are also typically utilized as higher band gap carrier blocking layers in LEDs [13].

While efficient red phosphide LEDs do exist, bridging the so-called *Green Gap* with nitrides would mean a great breakthrough, as comparably good alternatives in this color range are not yet available. Fundamentally, it would appear that III-nitrides are extremely useful for optoelectronics but many challenges still remain as green, yellow, red and UV nitride LEDs are noticeably lagging behind the original blue ones in terms of efficiency, with much effort being devoted to amend the matter.

Material quality obstacles are a main concern, much due to the lack of a practical and economical, bulk single crystal growth method, like the Czochralski process for Si. This nuisance necessitates GaN to be grown epitaxially onto substrates with different crystal structure, lattice constants and thermal expansion coefficients, causing lattice mismatch, strain and hard to suppress threading dislocations (TDs). These dislocations create many non-radiative recombination sites and scattering centers detrimental to the optical and electrical characteristics of the GaN [24]. Although different ways to improve GaN quality have been presented, often centered around the use of buffer layers, [14, 25, 26] a definitive solution to this issue has not yet been found. Today sapphire (α-Al_2O_3), Si and SiC among other materials, are used as substrates for GaN epitaxy but effectively matching material lattice constants, listed in table 2.1, remains a major issue for III-nitride development.

Table 2.1: Band gap and lattice data for the III-nitride compounds and other common materials in semiconductor processing at 300 K [27–31].

	Structure	E_g / eV	Gap type	Lattice constants / Å
GaN	Wurzite	3.39	direct	$a_0 = 3.189$, $c_0 = 5.186$
AlN	Wurzite	6.2	direct	$a_0 = 3.112$, $c_0 = 4.982$
InN	Wurzite	0.72	direct	$a_0 = 3.533$, $c_0 = 5.693$
Si	Diamond	1.12	indirect	5.43
SiC (6H)	Hexagonal	3.0	indirect	$a_0 = 3.081$, $c_0 = 15.117$
GaAs	Zincblende	1.43	direct	5.65
α-Al_2O_3	Hexagonal	8.8	direct	$a_0 = 4.76$, $c_0 = 12.99$

As if this was not tricky enough, nitrides are especially inclined to exhibit piezoelectric polarization due to their, compared to arsenic compounds such as GaAs, more than 10 times larger piezoelectric constants [32]. Piezoelectric fields are strain induced with their polarity being dependent on whether the strain is compressive or tensile and in turn, they will lead to something called the quantum-confined Stark effect (QCSE) [33]. The ideally rectangular band diagram of the tiny QW will now appear more triangular, causing electron and hole concentrations in it

to become increasingly spatially separated as shown in figure 2.3. In effect, this reduces radiative recombination rates and can cause emission peaks to redshift [34]. The QCSE is generally worse for green, yellow and red emitters due to the increased strain of having a higher In incorporation in the QW.

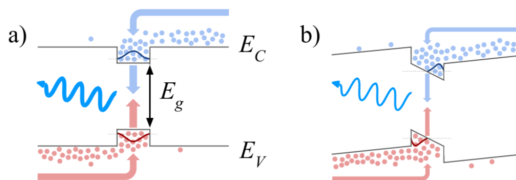

Figure 2.3: **a)** Band diagram of a LED with sufficient applied forward bias to completely flatten the bands. Carrier concentrations perfectly overlap and create intense emission. **b)** Accounting for the QCSE and carrier separation inside the QW.

To make matters even worse, the high quality InGaN films needed for the wells are highly non-trivial to form and exhibit a tendency to phase separate. When this happens under the right circumstances however, radiative recombination may actually be improved by quantum confinement effects, offering a possible explanation to why the blue nitride LEDs work so well [35]. Even as blue emitters can be made remarkably efficient, the EQE is generally degraded for higher currents in a phenomena dubbed the efficiency droop, mainly considered to be related to Auger recombination [36]. Finally there is the issue with low p-type GaN conductivity which has traditionally been one of the greatest challenges for nitride LEDs with only a small percentage of Mg acceptor atoms being effectively ionized at room temperature. Additionally, annealing steps have been shown to be necessary in order to reverse the effects of hole compensation by atomic hydrogen dissociated from NH_3 during epitaxy [18].

2.1.5 Platelets

To circumvent the material problems and create high quality GaN, a technique has been patented by Jonas Ohlsson and Mikael Björk [37]. It revolves around epitaxial, radial, outgrowth from the dislocation free, Wurzite GaN nanowire (NW) and a reformation phase to create tapered platelets with a planar top surface. This top surface, also called the c-plane, is polar and perpendicular to GaN crystal direction [0001]. Growing p-n junctions on this plane is how most commercial LEDs are fabricated while many nanostructure devices incorporate radially grown, core-shell, p-n junctions on non-polar m, and semi-polar s-planes [38–42]. The ability to grow more predictable InGaN layers is a significant advantage of using the c-plane [43] while both approaches feature effective filtering of TDs from the substrate below when based on selective area growth (SAG)

structures [44]. Using the c-plane is not entirely bother free however as LEDs based on this plane are more QCSE prone than m-plane devices [9].

GaN NWs can be grown by metalorganic vapor phase epitaxy (MOVPE) onto lesser quality GaN layers using SAG methods [45], improving the economics as inexpensive, mismatched substrates can be used to a greater extent [44]. Shown in figure 2.4 is a comparison between a radial p-n LED, similar to those produced by Lund University spin-off company Glo AB [46], and a c-plane, platelet LED, further explored in this work.

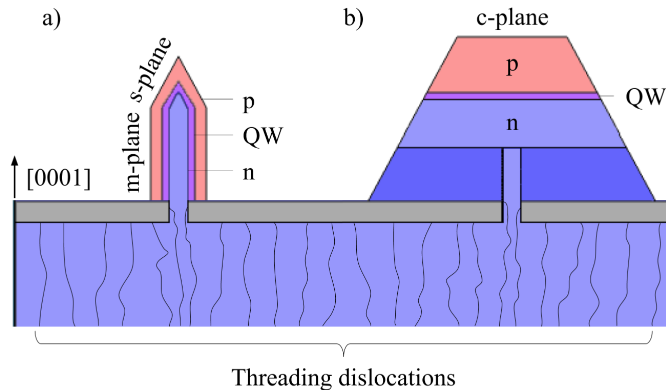

Figure 2.4: Cross sections of NW based LEDs. **a)** Radial/core-shell and **b)** platelet. Both devices are based on a SAG NW, filtering out TDs from the lower layer. QW thickness is exaggerated for both cases.

Platelets combine the use of the c-plane for device growth from proven planar LED technology with the perfect material quality of the NW. There is also the prospect of <1 µm diameter, individual devices, not yet possible to produce with conventional etch methods without risking considerable surface damage and reduced radiative efficiency. The possibility to make robust LED devices on this scale make the platelet method a promising candidate for high resolution optogenetics.

2.2 Optogenetics

Optogenetics is the collective name for technology relating to the control of biological events by optical stimulation [47]. It was discovered in 2005, that action potential spiking in mammalian neurons could be optically controlled by genetically altering cell membranes to express the 470 nm blue light sensitive, non specific cation channel, Channelrhodopsin-2 (ChR2), found naturally in green *Chlamydomonas reinhardtii* algae [48–50]. Although ChR2 stimulation is very dependent on light exposure time, it has been shown that action potentials can be generated by intensities as low as $1\,\mathrm{mW\,mm^{-2}}$ [51]. The approach enables targeting of specific cell types which is not possible with traditional electrode stimulus [47].

2.2.1 Neurons and action potentials

Neurons are excitable, signal-carrying and processing cells that constitute the main building block of the nervous system in animals, numbering around 86 billion cells in a single human brain [52]. The cell membrane incorporates ion channels to let through charged ions and transport pumps working metabolically to maintain the electrochemical, resting membrane potential. The potential across the membrane is locally affected by impulses from other neurons or interactions with extracellular systems and when it reaches a certain threshold, the accumulated, graded potential, can trigger an action potential at the axon hillock. The potential is now offset enough to open nearby voltage gated Na^+ channels, rapidly depolarizing the membrane, causing a chain reaction impulse to move along the axon as more voltage gated channels are opened. The depolarization overshoot causes the Na^+ channels to close and K^+ channels to open, setting in motion the repolarization of the membrane. After a refractory period, the resting potential is restored and ready for the next action potential to be transmitted [53]. Action potential characteristics as well as the basic features of a neuron are illustrated in figure 2.5.

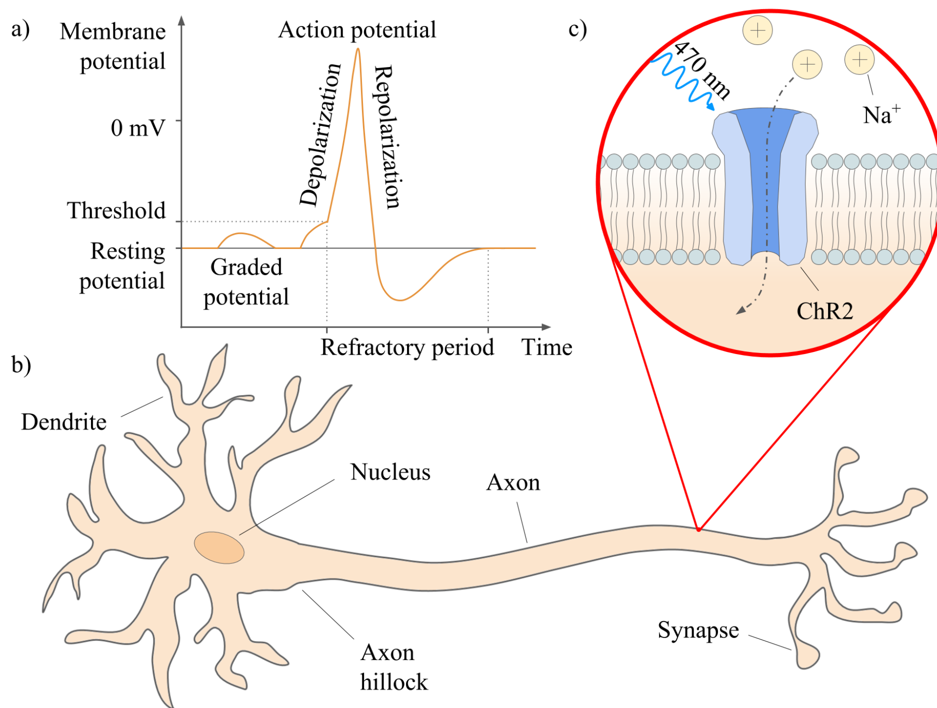

Figure 2.5: **a)** Membrane potential vs time graph illustrating the difference between graded and action potentials. **b)** Basic parts and features of a simple neuron. **c)** ChR2 ion channel over the cell membrane.

2.2.2 Epilepsy

Epilepsy is a collection of neurological disorders with the common factor of causing epileptic seizures [54]. The often unprovoked seizures are characterized by abnormal excessive or synchronous neuronal activity in the brain [55]. Estimated to affect 39 million people and to have caused 125 000 fatalities worldwide in 2015 [56, 57], the effects of the disease are grave, on individuals affected and society as a whole. While there is no cure, seizures can be controlled by medication in about 70 % of cases [58].

A possibility with optogenetics is to inhibit activity of targeted neurons so that the extent of epileptic seizures can be mitigated [59]. While significant challenges still exist to produce an optogenetic treatment for epilepsy the same principles can be applied to other neurological diseases where neuron activation is at the center of attention.

2.2.3 Patch-clamp technique

Patch-clamp is an electrophysiological technique that can be used to measure the membrane potential of individual cells. This is achieved by carefully attaching a micropipette probe containing intracellular fluid to the cell interior through its membrane. The pipette houses an electrode while the ground reference electrode is placed in the electrolyte medium surrounding the cells meant to simulate the extracellular space. Neuron electrophysiology requires continuous circulation of artificial cerebrospinal fluid (aCSF) to keep cells healthy and excitable for extended durations. Typically aCSF consists of NaCl, $NaHCO_3$, glucose, KCl, NaH_2PO_4, $MgSO_4$ and $CaCl_2$ with O_2 and CO_2 being added to the mix when the solution is bubbled. By using the technique for whole cell recording, illustrated by figure 2.6, action potentials of individual neurons can be recorded [60].

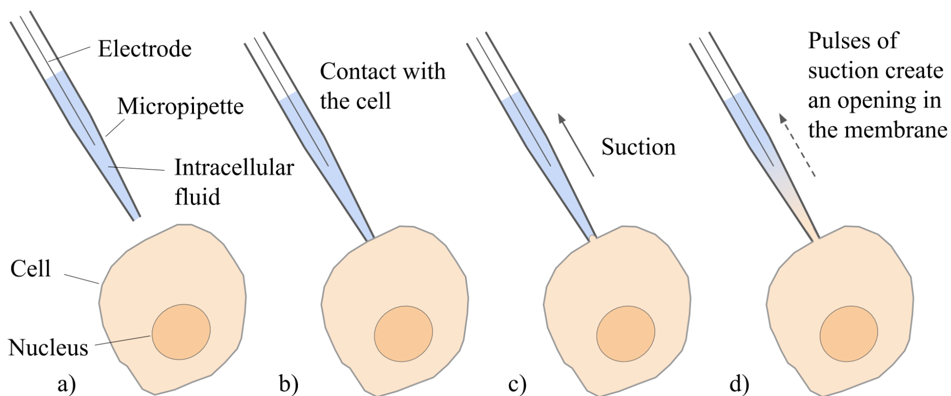

Figure 2.6: Patch-clamp setup steps for whole cell recording.

Chapter 3

Methodology

This chapter will cover techniques and methods used in the LNL ISO 5–8 cleanroom facilities to create µ-platelet LEDs, processing to pattern and connect these into experimental optogenetic light sources, device characterization and their packaging for a biological test environment.

3.1 Platelet synthesis

Starting off, it makes sense to give an overview of LED epitaxy, which I was not involved in other than requesting the substrate material, layer thicknesses and QW emission wavelength. I relied heavily on efforts of Taiping Lu, Zhaoxia Bi and Maryam Khalilian to supply raw platelet LED samples for my work.

Due to the constraints of the patch clamp rigs in the EEG lab at the Biomedical Centre, the LEDs needed to be based on a sapphire substrate, transparent for the built in transmission light, optical microscope setup. Sapphire wafers with MOVPE grown, n-doped GaN buffer layers were acquired from a commercial vendor and sent to a third party process facility where a 30 nm thin silicon nitride (Si_3N_4) growth mask layer was deposited by low pressure chemical vapor deposition (LPCVD). Plasma enhanced chemical vapor deposition could have been used for this step and is available in LNL, but LPCVD tends to result in less hydrogen incorporation [61]. At this point, the growth mask covered wafer was patterned by electron beam lithography (EBL) in-house, with nano imprint lithography being an available alternative method. Hexagonal arrays of 100 nm diameter holes, spaced 1 µm apart were transferred to the Si_3N_4 mask by reactive-ion etching (RIE) with CHF_3 plasma. The wafer was then diced into multiple 8×10 mm chips, each containing a 1.6×2.8 mm SAG hole array with around five million holes. The chips were finally cleaned to strip them of any remaining EBL resist before being ready for epitaxy. The cross sections of figure 3.1 illustrate the discussed substrate and array preparation steps.

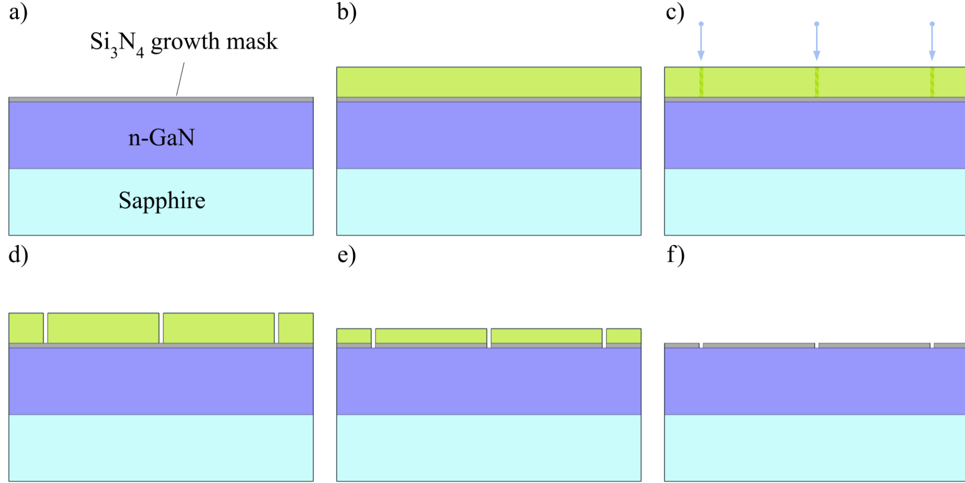

Figure 3.1: **a)** n-GaN on sapphire covered with Si_3N_4 by LPCVD. **b)** EBL resist spin coated. **c)** Array EBL exposure. **d)** EBL resist development. **e)** CHF_3 RIE. **f)** Resist stripped.

A sample chip would now be loaded into the LNL nitride MOVPE growth chamber for GaN NW epitaxy. Wires start forming at the base of the holes in the Si_3N_4 mask, on the exposed buffer n-GaN surface. They were grown to a height of about 450 nm, roughly keeping the predefined diameter of the mask holes, under flows of gaseous NH_3, N_2 and triethylgallium (TEGa) with a smaller flow of H_2. By changing growth parameters like temperature and pressure the NW formation can be altered to make them start growing out laterally towards an almost pyramid like shape. This step was followed by changing the parameters once more and removing the TEGa flow to reform the structures, in effect flattening them, to become approximately 80 nm tall, 600 nm top diameter, $60° \pm 2°$ sloped, hexagonal structures. These steps to create dislocation free, c-plane GaN, platelets are the main focus of the aforementioned patent [37] and will be more thoroughly addressed in coming papers by Maryam Khalilian and Zhaoxia Bi.

With a defined c-plane, epitaxy of the active device layers could commence. The n-GaN layer is ideally grown with flows of NH_3, N_2, TEGa and SiH_4. However, during the project there were issues with the SiH_4 gas supply, necessitating growth of n-GaN without active n-type doping, the main purpose of SiH_4. Fortunately, unintentional background doping inside the reactor typically makes grown GaN n-doped anyway. The resulting donor concentration N_D is believed to have been between 10^{16} and $10^{17}\,\mathrm{cm}^{-3}$, short of the 3–$5 \cdot 10^{18}\,\mathrm{cm}^{-3}$, aimed for range with active SiH_4 doping. The n-GaN was grown to a thickness of approximately 30 nm. Next layer, was the 3–4 nm thick $In_xGa_{1\text{-}x}N$ QW with the In content fraction, x being between 0.16 and 0.18. The chosen composition corresponds to the ideal light emission peak at $\lambda = 470\,\mathrm{nm}$ for maximum ChR2 response. The layer was grown under flows of NH_3, N_2, TEGa and

trimethylindium. The last epitaxial layer was the p-GaN layer and for it, instead of the indium precursor, bis(cyclopentadienyl)magnesium was used to add p-type dopant, Mg impurities to the crystal. This layer was grown to a relatively large thickness of 130–150 nm, considerably simplifying later processing steps. The target acceptor impurity concentration N_A was in the range of $2–5 \cdot 10^{19}\,\text{cm}^{-3}$ however, actual p-type conductivity would still have been very poor at this stage. Cross sections after each MOVPE process step are depicted in figure 3.2.

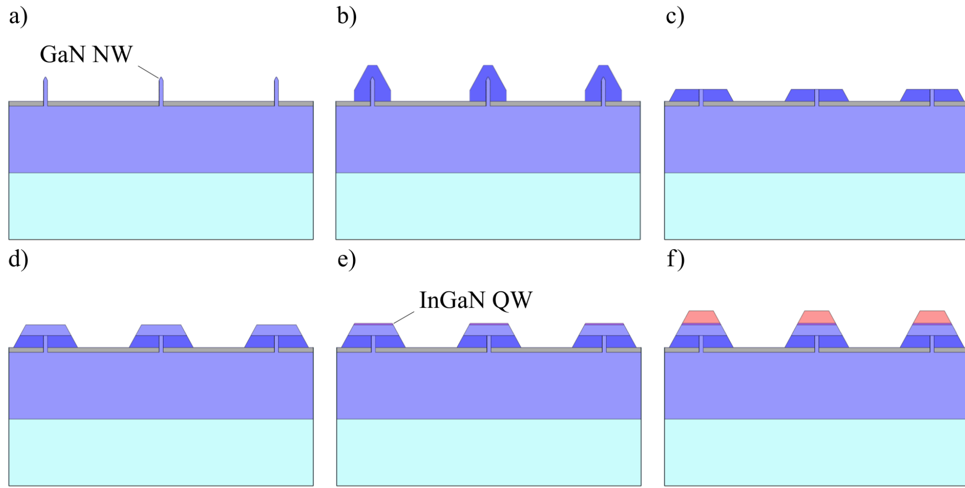

Figure 3.2: **a)** GaN NW epitaxy. **b)** Lateral GaN growth. **c)** Reformation phase. **d)** n-GaN layer. **e)** InGaN QW layer. **f)** p-GaN layer.

3.2 LED processing

With platelet epitaxy complete, my lab processing efforts commenced. The steps, already developed in the nitride group, to individually and accurately connect platelet LEDs with lithography and thin film techniques [62] would form the basis for my work to create an optogenetic LED device.

3.2.1 Rapid thermal annealing

In order to activate the Mg, p-type dopants and achieve a sufficiently high hole conductivity, a 10 min, 700 °C rapid thermal anneal was performed under N_2 flow. The annealing was either performed in the UniTemp RTP-1200-100 tool or *in situ*, in the MOVPE reactor, approximately activating 1 % of acceptors to achieve a free hole concentration p around $2–5 \cdot 10^{17}\,\text{cm}^{-3}$. Note that activation needs to yield higher concentration than the background, typically n-type, doping discussed in section 3.1 to get actual p-type material.

3.2.2 Atomic layer deposition

Atomic layer deposition (ALD) was used to cover the chip, including platelet surfaces, with a thin layer of aluminium oxide (Al_2O_3) in the Cambridge NanoTech, Savannah-100 tool. It works by having gas pulses of the precursors, trimethylaluminium and H_2O relieve each other to create a single monolayer of amorphous Al_2O_3 per cycle. A total of 300 cycles were run at 300 °C forming a roughly 30 nm thick layer, which was verified by ellipsometry on a simultaneously covered Si reference chip. A single Al_2O_3 monolayer should therefore be approximately 1 Å thick. In contrast to α-Al_2O_3, which is crystalline, Al_2O_3 films deposited by ALD are amorphous unless annealed at crystallization temperatures exceeding 1 000 °C [63]. ALD with following spacer layer and UV lithography cross sections are shown in figure 3.3.

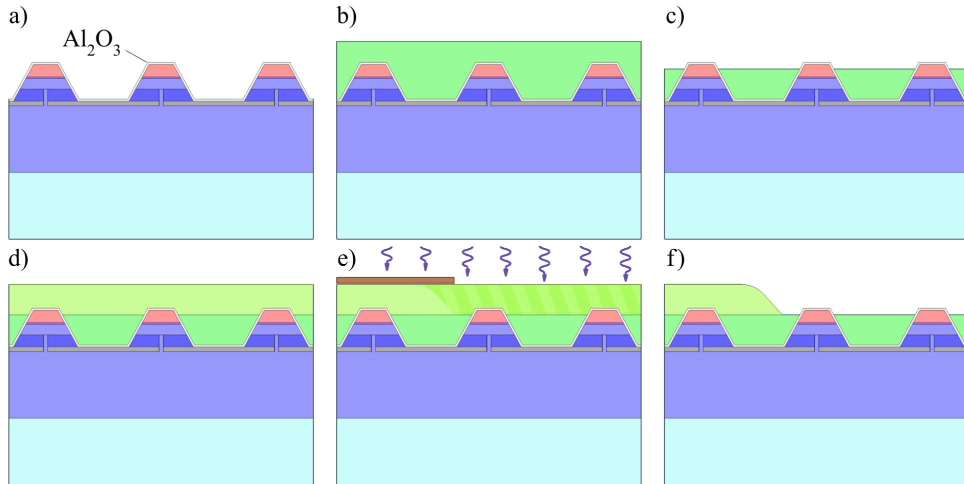

Figure 3.3: **a)** Al_2O_3 ALD layer. **b)** S1805 resist spin coated and hard baked. **c)** O_2 RIE. **d)** S1813 resist spin coated. **e)** UV exposure. **f)** Resist development and hard bake.

3.2.3 Spacer layers

To create a device surface where only the p-GaN surface was exposed and later connected with a metal anode contact, a spacer layer of Microposit S1805 G2 photoresist was utilized. The resist was spin coated onto the chip at 3 000 rpm for 60 s and hard baked at 250 °C for 10 min to make it permanent. According to the material data sheet, the coated layer should be around 550 nm thick [64] but since the surface is structured and not planar, the actual thickness would likely vary. Next step was to etch away the resist just enough to expose the platelet tops by using the Trion Sirus T2 RIE with 15 SCCM O_2 flow, 300 mTorr pressure and 50 W radio frequency power. This is where the thick p-GaN layer matters, as the growth height uniformity of the platelet technique is not yet fully perfected. The thick layer allows more platelet p-sides to be connected separately

from the n-sides and reduces the probability of short circuiting diodes. Samples exhibited resist height variations over the whole array, likely due to uneven coating and minor epitaxy related variations, especially visible close to discontinuities in the array pattern. In this case, as shown in figure 3.4, the uniformity issues can be explained by an abundance of growth precursors from nearby regions with few or no growing structures, increasing the growth rate of the structures that exist. The resist etch method used to reach the sweet spot range for as many platelets as possible was by iteration of 60–90 s O_2 etching steps and checking the progress in the Hitachi SU8010 scanning electron microscope (SEM). This process is visualized in figure 3.4.

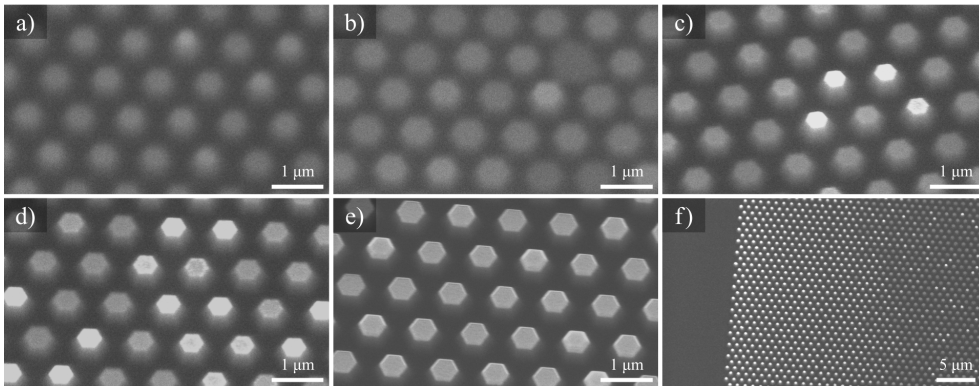

Figure 3.4: **a)-e)** Angled scanning electron micrographs of platelets after consecutive O_2 RIE runs where all are completely covered by resist in **a)** and most are exposed and ready for further processing in **e)**. **f)** Irregularities in growth height of platelet structures near the array edge.

The next step was to add an additional spacer layer, padding eventual contacts and bond pads to further protect against short circuiting. This is relevant as the only thing protecting the n-side GaN otherwise would be the etched down S1805 layer plus the 30 nm film of Al_2O_3 and the Si_3N_4 growth mask. This next spacer layer would ideally end up covering most of the the sample area except for a thin trench, patterned by UV lithography, where LEDs were to be contacted. The chip was preheated to 115 °C on a hotplate, had Microposit S1813 positive photoresist spin coated onto it at 3 000 rpm for 60 s and was soft baked at 115 °C for 90 s. The chip was then mounted in the SUSS MicroTec, MJB4 mask aligner and aligned to a 20 µm strip with hourglass shaped ends, chosen from the several different strip widths on the mask. The sample was exposed to 365 nm UV light in the soft contact mode for 10.5 s amounting to a total dose of 210 mJ cm^{-2}. The resist was developed for 70 s in Microposit MF-319 developer and quickly rinsed in Milli-Q purified, deionized water (DIW). With exposed areas removed, since S1813 is a positive resist, the sample was hard baked for 15 min at 250 °C similarly to the S1805 layer.

3.2.4 Etch hole definition

Following the use of UV lithography to transfer large scale, comparatively low resolution patterns, EBL was adopted to define the fine patterns and features to precisely contact individual, single platelet diodes. Poly(methyl methacrylate) with molecular weight 950 000 g mol^{-1}, 6 % formulated in anisole (950 PMMA A6) was spin coated onto the chip at 3 000 rpm for 45 s. The sample was then baked at 180 °C for 2 min before being loaded into the Raith Nanofabrication, Voyager EBL tool. The purpose of this lithography step was to create a pattern for etching away the Al_2O_3 layer from platelets to be connected. Figure 3.5 represents a continuation of previous cut through process sketches and illustrates etch hole definition.

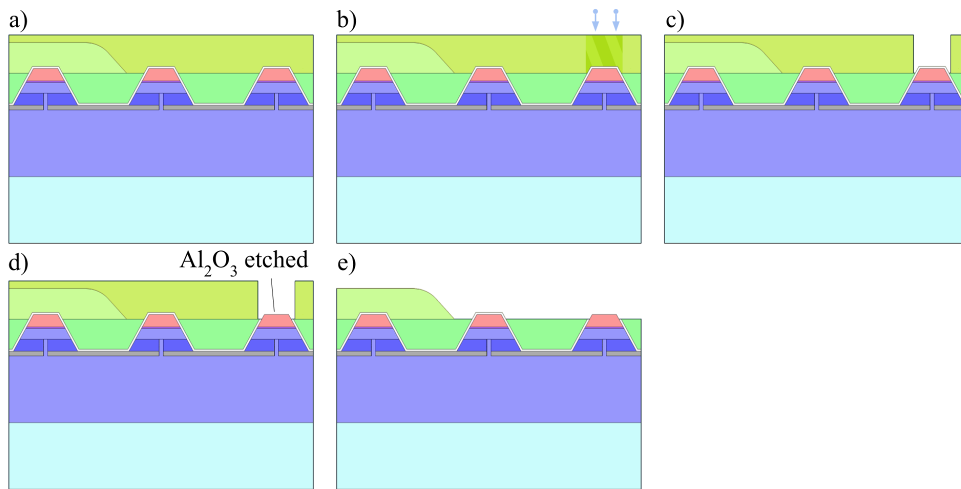

Figure 3.5: **a)** 950 PMMA A6 resist spin coated. **b)** Etch hole EBL exposure. **c)** Resist development. **d)** Uncovering platelet tops with BOE. **e)** Resist stripped.

The tool was aligned using the built in SEM functionality with great care to avoid unintentional resist exposure and cross linking. Array geometry and optical microscope distance mapping was used to align the exposure pattern without having to view the particular area of the chip about to be exposed. With alignment checked and position lists containing the 400 × 400 µm write field (WF) design patterns set up, exposure could commence with 50 kV acceleration voltage, 4 nm step size and 500 µC cm^{-2} dose using a medium condenser and 40 µm aperture mode. Due to minor offsets in the array, pattern realignment was occasionally required while switching to the next WF. The etch pattern was most commonly defined as a 1 µm straight line, etch row but experimental designs with varying dimensions were also used.

Post electron beam exposure of the etch holes the resist was developed for 90 s using the metyl isobutyl ketone (MIBK) and isopropanol (IPA) blend 1:3 MIBK:IPA for highest pattern resolution [65] and a 20 s IPA dip to remove any remaining developer. J.T.Baker buffered oxide etch

(BOE), 10:1 NH_4F buffered and DIW diluted HF solution, was used to wet etch Al_2O_3. Etching for 60 s with a rate of 6 Å s^{-1} should over etch by about 6 nm and safely uncover exclusively the p-GaN, platelet tops. Immediately after etching the chip was dipped into two separate beakers of Milli-Q purified DIW to remove any remaining BOE. In preparation for contact definition EBL, the remaining PMMA resist was stripped by placing the sample in acetone for around 60 min and rinsing it in two beakers of IPA for 10 plus 30 s. Etch hole and similarly obtained contact definition patterns are presented in figure 3.6.

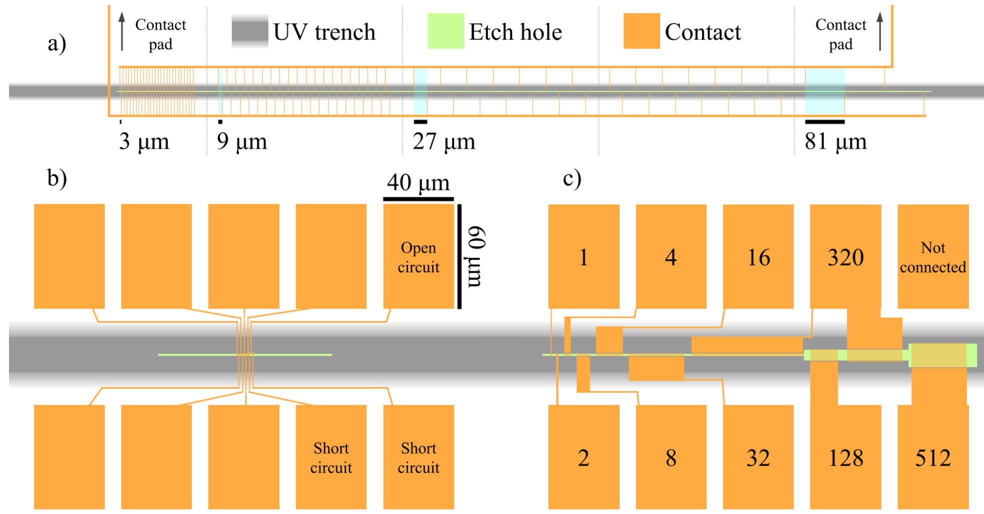

Figure 3.6: EBL patterns for **a)** the prototype optogenetic device stretching over five WFs with 3 to 81 µm separation between top and bottom connected platelets, **b)** single platelet LEDs with open and short circuit test contacts and **c)** parallel platelet LEDs of increasing size from a single platelet to 512 connected in parallel. Due to incorrect design file associations the pattern featured a 320 platelet diode and an unconnected pad instead of the planned 64 and 256 platelet LEDs.

3.2.5 Contact definition

In the exact same fashion as for etch hole definition, 950 PMMA A6 was spin coated onto the chip and baked. Before loading into the EBL tool however, a scalpel was used to create a ground, scratch contact close to the edge of the chip by digging through the resist and thin film layers burying the n-GaN buffer. Using the same EBL settings as for the etch holes, contact patterns were exposed. Significantly longer exposure times were observed mainly due to the large contact and bond pad patterns but also because of the multiple overlapping WFs used to extend contact lines to the chip edges. Figure 3.6 shows the exposure area difference quite clearly and how coinciding contact and etch row patterns allow for creating single platelet and larger parallel platelet LEDs.

The principle behind the optogenetic prototype design, also shown in

figure 3.6, was to create a simple device with only two parallel connected diode rows out of a single long line of platelets. As all parallel connected platelets would light up simultaneously, optogenetic resolution would be achieved by controlling the light intensity so that only the one emitter closest to the neuron would contribute to a cell response. Resolution would furthermore depend on the separation of light sources and this is why the distance between closest connected platelets is graded from 3 to 81 µm. This approach was favored mainly due to connection simplicity and the higher likelihood of neurons attaching to the chip in such a way that they would overlap the LEDs as a larger surface area would be covered than by using only a few single platelet diodes. The subject of the device design is revisited in chapter 5. Final process step cross sections, in figure 3.7 depict device completion from contact definition to ALD passivation.

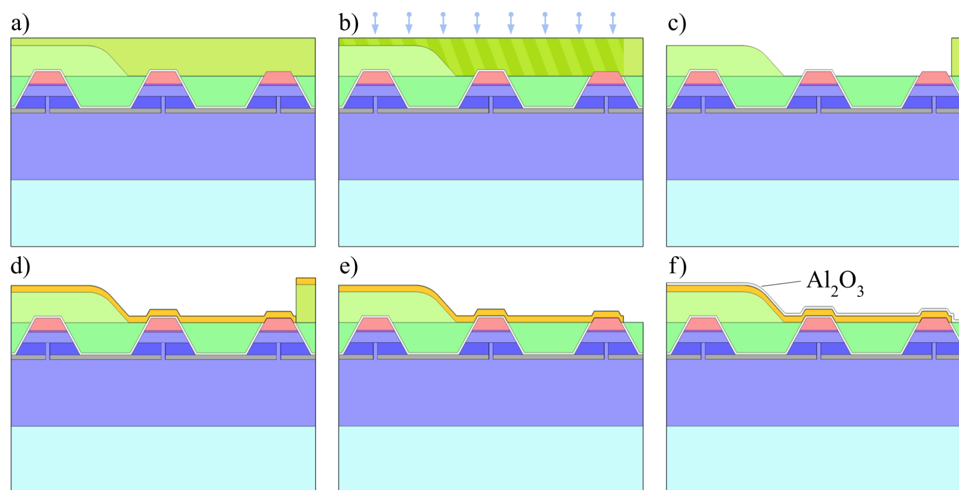

Figure 3.7: **a)** 950 PMMA A6 resist spin coated. **b)** Contact EBL exposure. **c)** Resist development. **d)** Ni and Au evaporation. **e)** Lift-off. **f)** Al_2O_3 ALD passivation layer.

After developing the PMMA resist with MIBK and IPA for a second time the similarities with the etch hole definition come to an end. The chip was now mounted in the Pfieffer Vacuum Classic 500 evaporator and had a 5.5 nm Ni layer followed by a 100 nm Au layer deposited onto it by thermal evaporation. Ni/Au bilayers are often used to create an ohmic contact to low conductivity p-GaN [66], however the thick Au film used to create sturdy contact pads is also completely opaque to visible light. Redundant metal was removed with a lift-off process using Microposit Remover 1165 heated to 80 °C on a hot plate. Occasionally a bottle was used to spray the chip to hurry the process, still taking around 45 min to complete. As a last action the chip was dipped in DIW and IPA. Figure 3.8 shows a 3D view of single platelet LEDs post lift-off.

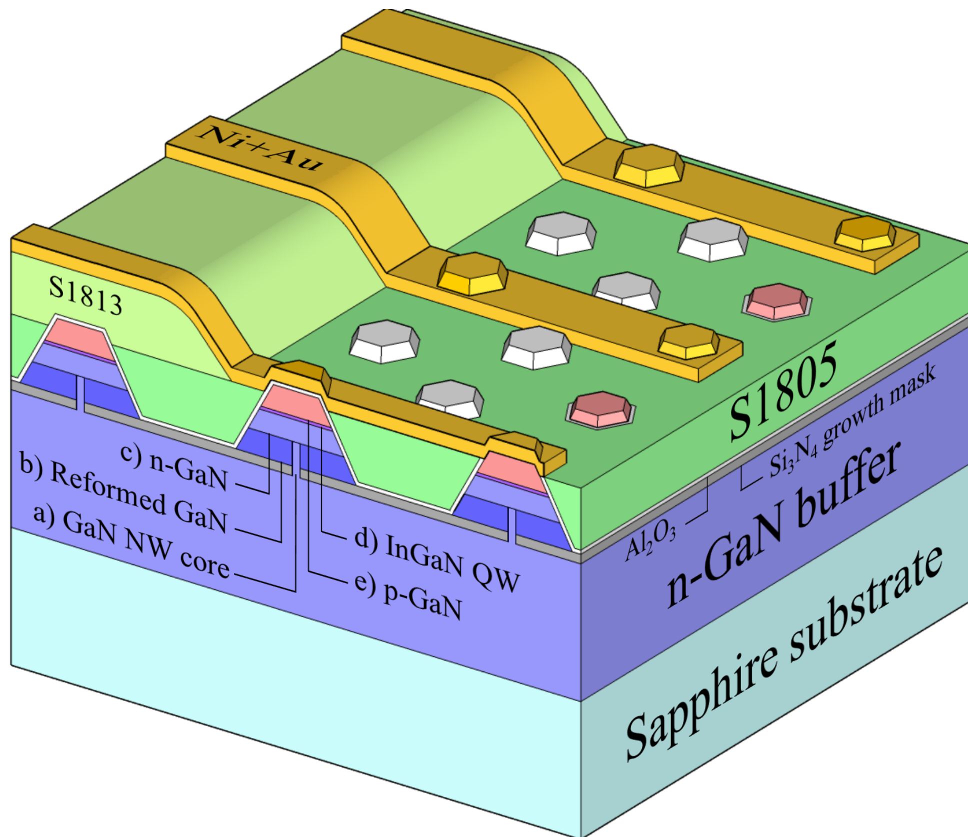

Figure 3.8: Single platelet LEDs post lift-off. Note that only the rightmost cross sectioned diode is connected with to the top metal contact as the center diode is being insulated by the thin Al_2O_3 layer and the leftmost diode by the Al_2O_3 and S1813 resist spacer layers.

3.3 Characterization

This section describes the main methods used to characterize devices. Results from characterization are presented in chapter 4.

Optical microscopy was used to verify pattern transfer and lift-off but also to capture other visual features up to 100 times magnified. For higher magnifications SEM was instrumental in characterizing individual platelet size and their connection to the top side metal contact. Figure 3.9 contains some electron and optical micrograpghs of the processed device.

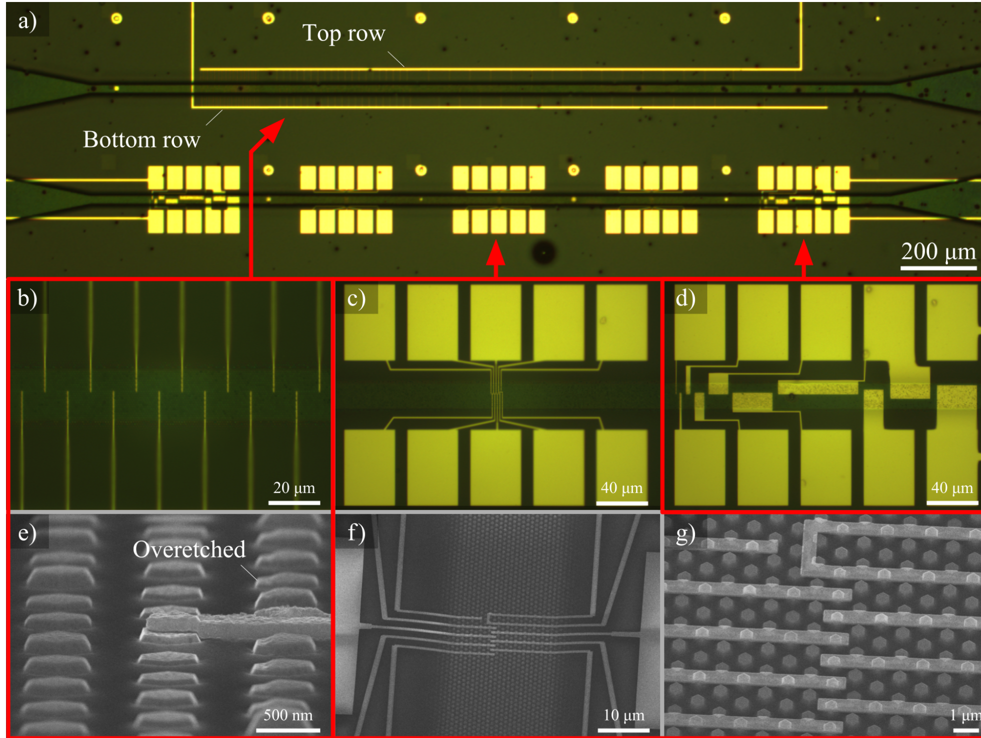

Figure 3.9: **a)** Optical micrograph over the device area with the five WF long optogenetic rows above three center single platelet patterns with the two outer WFs featuring parallel platelets. Bond pad, contact lines extend from both optogenetic rows and the four outermost contact pads of the parallel patterns. **b)** Magnified view of the optogenetic rows in the 9 µm emitter separation WF. **c)** Single platelet pattern. **d)** Parallel platelet pattern. **e)** Electron micrograph of a solitary optogenetic row platelet emitter. Note that Al_2O_3 appears to be etched on parts of the adjacent row, toward the contact in the image. **f)** Less angled SEM image of single platelet LEDs. **g)** Zoomed in view of **f)**.

Electrical measurements were performed in the Cascade Microtech Summit 11000B probe station connected to the Keithley 4200-SCS Semiconductor Characterization System, source measure unit (SMU). Probes were placed on the EBL defined contact pads and ground scratch contacts to capture I-V characteristics for the LEDs. An empirical method, using gradually ramped up direct current (DC) was used to improve diode I-V and encourage LEDs to light up without degrading their rectifying characteristics. Most I-V measurements were performed by sweeping the voltage from some negative voltage around -5 V to between 5 to 10 V in steps of 50–200 mV while recording the current for each step.

Emission spectra for the optical characterization was obtained using an Avantes AvaSpec-3648 fiber spectrometer. The fiber was positioned by using a modified probe micromanipulator so that spectra from a single platelet LED could be collected while the chip was completely enclosed on the probe station chuck. The very low ambient, dark side spectrum that

was detected by the spectrometer was subtracted away. An integration time of 60 s was necessary for low currents but ramping up eventually got the spectrometer saturated, forcing the use of shorter integration times.

3.4 Packaging

To recap, the main goal of the project was to optically stimulate and measure the response of primary neurons grown in close proximity to light emitters on a µLED chip. Because of this, devices needed to be packaged and biointegrated for a electrophysiological test environment. Passivating the LEDs was deemed necessary to protect electric conductors from shorting by the aCSF as well as to protect the cells from leaking currents and heat. In this section the steps performed to package the first prototype devices are presented. The methods were highly experimental and suggested improvements too these, based on the results and acquired experiences, are discussed in chapter 5.

To fit the LEDs in the EEG patch clamp rig a biointegration scheme involving mounting the 8×10 mm chip on a 30 mm diameter, borosilicate, cover glass disc was implemented. The glass disc would incorporate metal fields connecting the chip, via wire bonds, to an external current source. These fields were evaporated onto the discs through a shadow mask created using a Zortrax M200 3D printer. Most often, metal deposition would be done concurrently with device chips to save time, material and crucible wear, leading to the same 5.5 nm Ni and 100 nm Au layers being deposited on both. Next the chip was attached to the glass disc by a homemade technique using a small amount of S1805 resist as glue and hard baking the sample for 10 min at 250 °C.

A Kulicke & Soffa 4523D ultrasonic wedge wire bonder threaded with 25 µm Al wire was used to create electrical connections to the chip. Wire bonds were made from the evaporated Au fields on the glass substrate to the EBL defined, dragged out bond pads and scratched cathode contact on the LED chip. Getting the bonds to stick proved unexpectedly complicated with about one in twenty attempts being successful, causing excessive stress to the 150×150 and 250×250 µm chip bond pads. Repeated attempts at bonding the same area causes visual damage to the barely 100 nm thick contact fields and chip bond pads, sometimes resulting in the metal being locally removed. Eventually the two optogenetic device rows, the unconnected contact pad and the 512 platelet LED from the second parallel pattern as well as two ground scratch contacts, were bonded to.

To passivate the LEDs, contacts and wire bonds an approach relying solely on ALD was used due to the inherent ability to cover surfaces conformally. Al_2O_3 was the material of choice because of its potential as a thin and effective permeation barrier [67] while still being highly biocompatible [68]. In contrast to the previous use of ALD, this time 400 cycles were run, expected to equate to an approximately 40 nm thick layer covering the chip, glass substrate, metal fields and wire bonds all alike. A

slightly different recipe with longer pulse and in between N_2 purge time was utilized for deposition at 250 °C to reduce the risk of damage to the hard baked resist layers already incorporated.

To contain the ≈1 mL volume of aCSF prefered for cell growth and patch clamp recording, an acrylonitrile butadiene styrene, plastic pool rim was 3D printed. The 1 mm thick and 4 mm tall rim had an inner diameter of 24 mm for it to surround the device chip and wire bonds while leaving some Au contact area open for external contacts. The rim was glued in place with Sylgard 184 Silicone Elastomer, two component, encapsulant. Minor mechanical scratching was required to get through overspread encapsulant and Al_2O_3 covering outer contact areas. Figure 3.10 shows the completed device package.

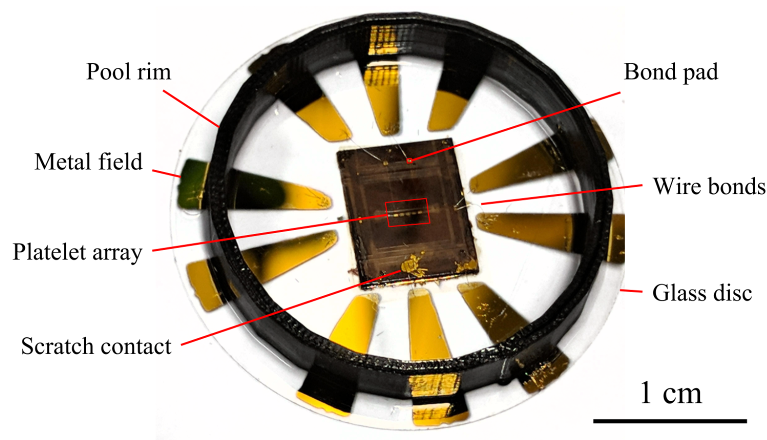

Figure 3.10: Finished device package and the physical counterpart of the computer created model in figure 1.1. Raw image courtesy of Daniel Jaghobi.

Chapter 4

Results

Results from characterization and testing are presented in this chapter. All measurements and tests were performed at room temperature, in atmospheric pressure and exposed to ambient lighting with the only exceptions to this being the EL spectra which were captured in the dark.

4.1 Current-voltage characteristics

A large number of semi-logarithmic, single platelet I-V characteristics were recorded and after seeing the diode curves become steeper and smoother with each new sweep, a technique was established to reliably improve the electrical properties of the LEDs. Figure 4.1 illustrates this process by which gradually increased DC runs would reduce the voltage required to keep the current stable.

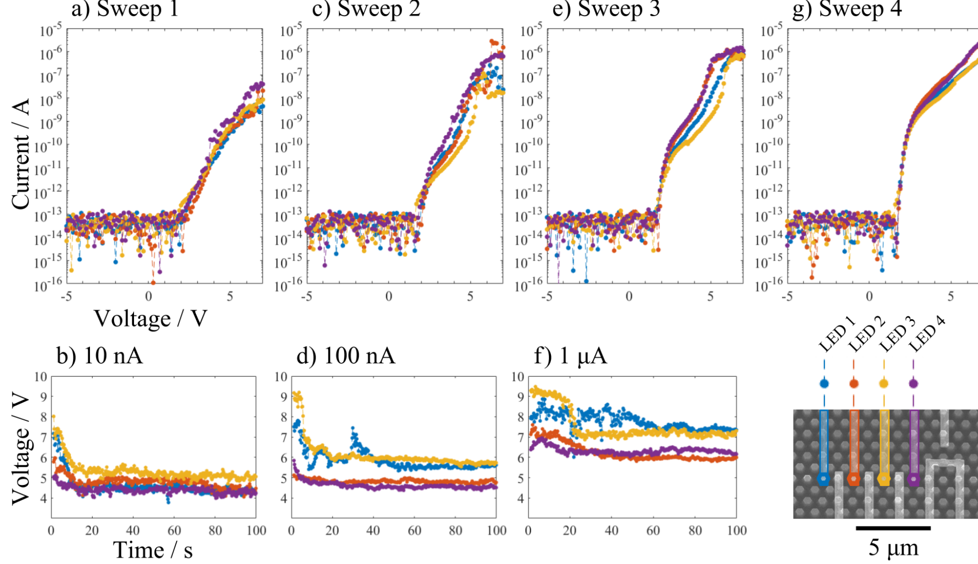

Figure 4.1: **a)-g)** Plots of chronologically ordered I-V sweeps and 100 s, increasing current, DC runs for four LEDs in the rightmost single platelet pattern of figure 3.9. Note that the legend SEM image is of another identical pattern and that pre-threshold current is below the SMU noise floor.

The high values for current density J, calculated with equations 4.1 and 4.2 provide a feasible explanation for the improved performance by current induced contact annealing. Under the assumption that quantum well and metal to p-GaN interface are roughly equivalent in area the densities achieved are conceivably enough to result in high local temperatures, p-contact annealing and reduced device series resistance R_S.

$$A = \frac{3\sqrt{3}}{8} D^2 = 211\,000\,\mathrm{nm}^2 \tag{4.1}$$

$$J = \frac{I}{A} = 474\,\mathrm{A\,cm}^{-2} \tag{4.2}$$

where A is the regular hexagon area of the QW, D its 570 nm long diagonal and I a current of 1 µA.

The necessity to incrementally increase the current was made obvious by broadening the sweep range as attempting to stress fresh diodes with longer sweeps caused them to degrade and more often lose rectification.

The contact annealing technique however, did not exclusively deliver desirable results as the I-V for LED 4 in figure 4.2 shows with a distinct jump at the end of sweep 5 toward higher current levels. Other than this exception, diode curves appear to keep improving, with LED 2 exhibiting exceptionally high current densities just shy of $50\,000\,\mathrm{A\,cm^{-2}}$ for $10\,\mathrm{V}$, albeit only for a short duration.

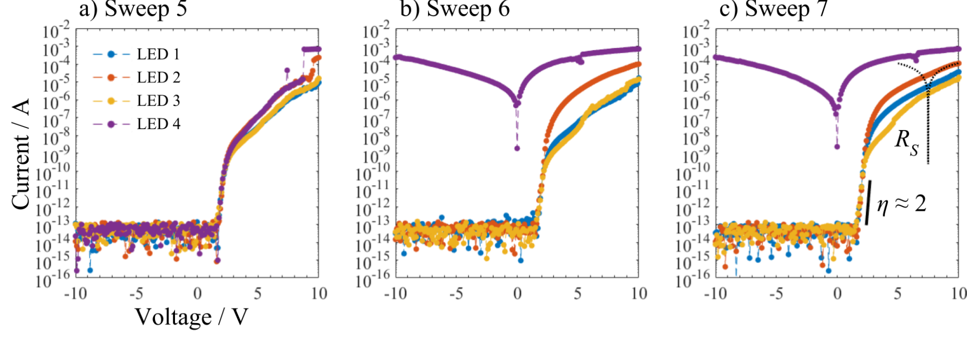

Figure 4.2: **a)-c)** Longer I-V sweeps of the devices in figure 4.1. Notice the deteriorating rectification for LED 4. **c)** $R_S \approx 22.5\,\mathrm{k\Omega}$ and $\eta \approx 2$ are estimated from limited voltage range, linear fit data for LED 2.

From the sweeps it is evident that the diode current levels emerge from the measurement setup noise floor at around $2\,\mathrm{V}$. The weak rectification observed for LED 4 seems to indicate that a non ohmic, Schottky contact forms directly between the p-side metal and the n-GaN, shorting the device. For LED 2, the resistance $R_S \approx 22.5\,\mathrm{k\Omega}$ was extracted from the I-V slope at higher voltages where the exponential increase in current is downgraded to a linear one [13]. This relatively high, lowest value for series resistance is likely due to the thick, low conductivity p-GaN layer. Similarly to R_S, the diode ideality factor η was evaluated from the I-V slope but this time from the steep region around $2\,\mathrm{V}$. Equation 2.3 was modified into equation 4.3 for this purpose.

$$\eta = \frac{e}{kT} \frac{1}{\frac{\mathrm{d}}{\mathrm{d}V} \ln I} \approx 2 \tag{4.3}$$

Moving on, the ohmic, short circuit contact I-V slope in figure 4.3 corresponds to roughly $97\,\Omega$ while the open circuit sweep reveals some minor leakage emerging out of the noise floor between 8 and $9\,\mathrm{V}$. Considering the $30\,\mathrm{nm}$ thin Al_2O_3 layer, electric fields could exceed $3\,\mathrm{MV\,cm^{-1}}$, opening the window for less conventional means of electron transport through the oxide, with Frenkel-Poole emission being a possible candidate [69]. This effect is only visible in the forward direction due to leaking platelets, still being perfectly functioning rectifying diodes. Although conditions should not allow any noticeable quantum tunneling it can not be completely excluded as a possibility due to defect conduction paths closing the distance.

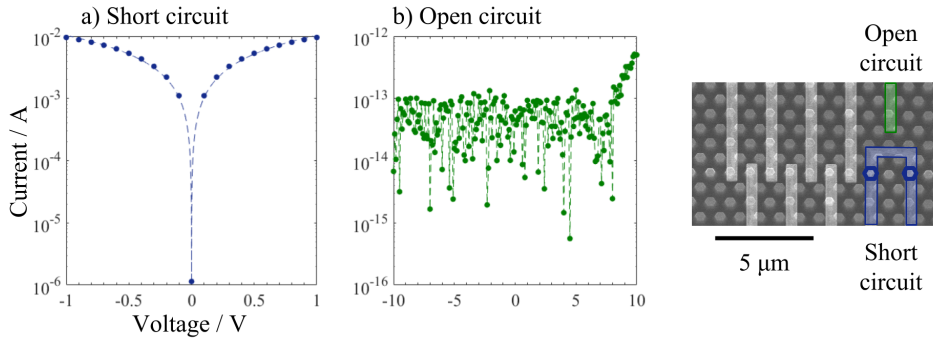

Figure 4.3: **a)** Short circuit test reveals a resistance of about 97 Ω by fitting the data points linearly. **b)** Open circuit test with small forward bias leakage. Both test structures are located in the rightmost single platelet pattern with the legend image once again depicting another pattern.

To study the effects of inhomogeneous platelets and processing, parallel diode I-V characteristics were measured and compared with high angle SEM images. The rationale behind the uniformity concerns, also discussed in section 3.2.3, relates to accidentally short circuiting the n-GaN with the metal contact. More platelets connected in parallel should in this case significantly increase the likelihood of creating a shorted circuit due to small device geometry variations which is corroborated by the I-V plots and device micrographs in figures 4.5 and 4.6. In these figures we see a tendency for diodes to become shorted, with worse rectification as a result, if they happen to include individual tall platelets.

After testing earlier prototype chips, holes in the metal layer were occasionally seen just above connected platelets as if they had erupted and done to the diode rectification what Vesuvius did to Pompeii, testifying to the presence of intense local heating and material deformation. Figure 4.4 displays examples of this occurrence and perhaps it is this deformation we should blame for short circuiting diodes which would have been healthy and strongly rectifying initially.

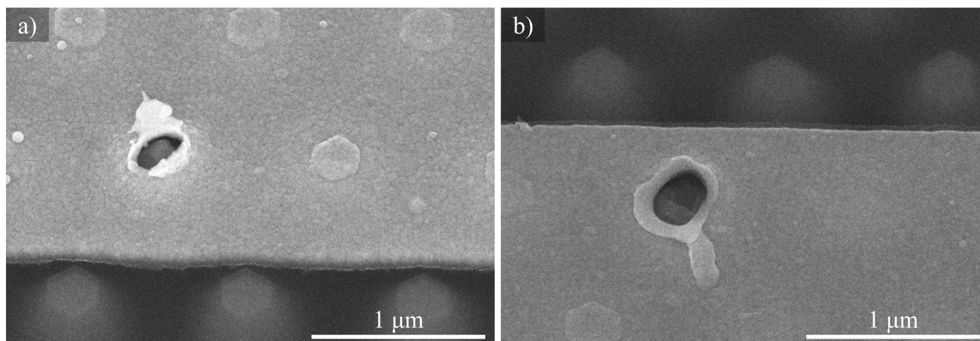

Figure 4.4: Examples of contact damage on a previous LED chip, parallel pattern.

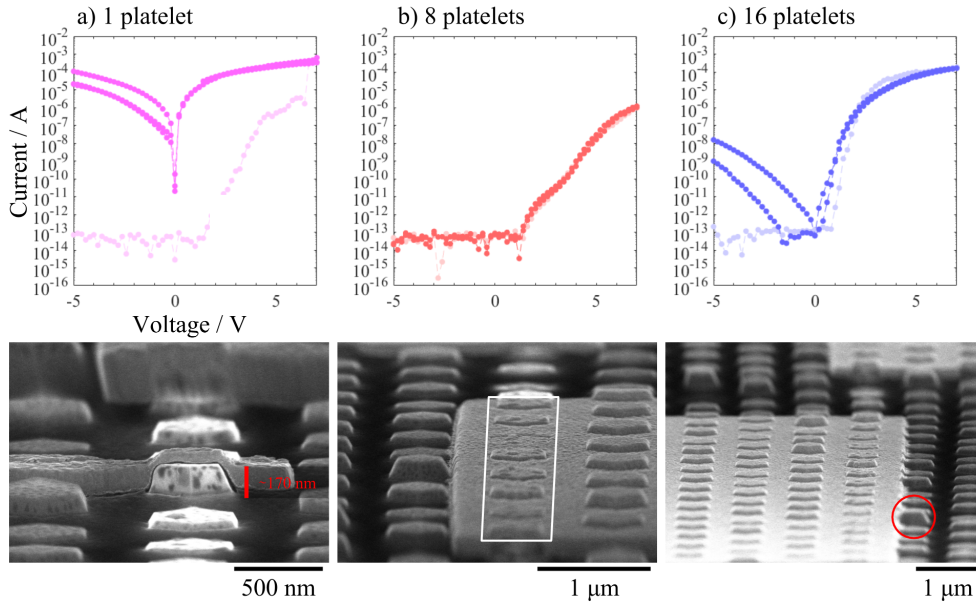

Figure 4.5: **a)** Tall single platelet device with close to symmetric logarithmic I-V plotted in pink. **b)** Rectifying 8 parallel platelet device. **c)** Less rectifying device with 16 platelets connected in parallel, just enough misaligned to have the metal contact cover the next row where at least one very high platelet is found. Lighter shade curves represent first sweep. The devices are all found on the leftmost parallel platelet pattern in figure 3.9.

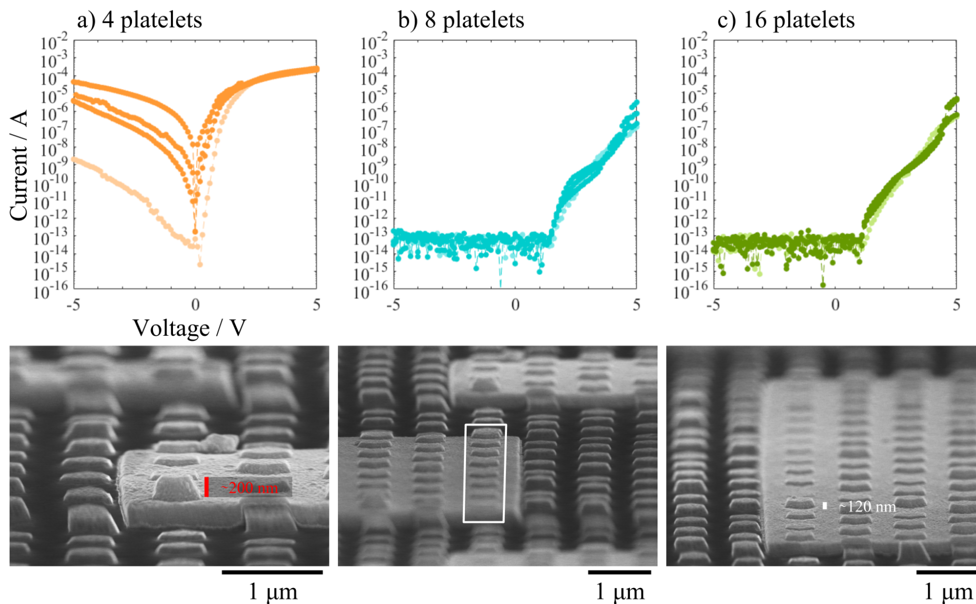

Figure 4.6: **a)** Deteriorating rectification for the 4 platelet pattern clearly featuring one very tall platelet. **b)** Eight platelets rectifying. **c)** Sixteen platelets also rectifying. These devices are from the rightmost parallel pattern in figure 3.9.

Since the two optogenetic row devices were basically just parallel connected diodes spaced further apart, the same issues with rectification should be present. EBL contact definition aimed to connect a total of 62 platelets per row, however as there was no fourth WF etch row exposure, a maximum of 55 platelets would eventually be connected. The devices did indeed turn out to be not very rectifying as shown by figure 4.7.

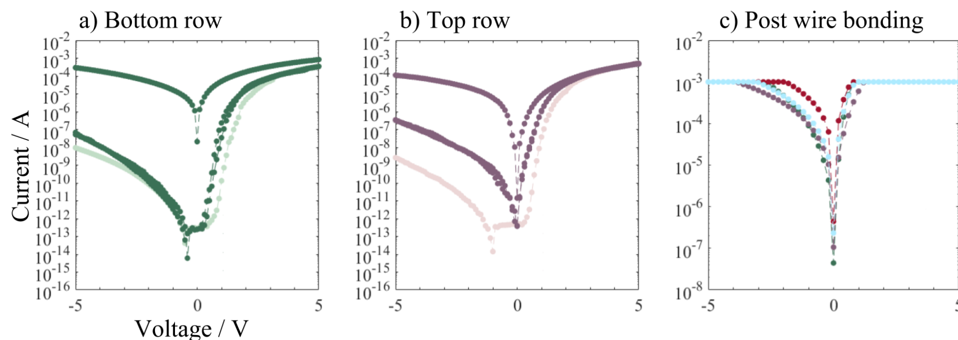

Figure 4.7: **a)-b)** Optogenetic row I-V with the lighter shade curves representing the first sweep. **c)** All four wire bonded devices short circuited through the bond pads. SMU compliance is set to 1 mA.

Also shown in figure 4.7 are the I-V results after wire bonding from the chip bond pads to the glass substrate. Unfortunately, the bonding punched through all protection to the buried n-GaN buffer layer, effectively shorting the device. The main reason for this was the UV mask peripheral features coinciding with the EBL defined bond pads, making them only partially padded by the S1813 spacer layer. With the experiences gained, future attempts will likely be more successful at connecting devices in this fashion. While the short circuit path of significantly lower resistance eliminated diode light emission, some consolation was found in the fact that device light up patterns could be recorded before wire bonding and packaging was performed.

4.2 Electroluminescence

So far the I-V symmetry issue has received much attention but for an optogenetic device there only really needs to be light emission which there was a lot of. Even for most shorted diodes, the measured spectra was similar to that of the rectifying single platelets but obviously quantities like the EQE will be worse due to the leaking shunt current path.

Single platelet EL spectra are shown in figure 4.8 while figure 4.9 contains pictures of emitting LEDs. The peak, full width half maximum (FWHM) was determined to be around 24–35 nm in the tested current range while a 15–17 nm blueshift was recorded going from 0.5 to 5 µA as presented in table 4.1.

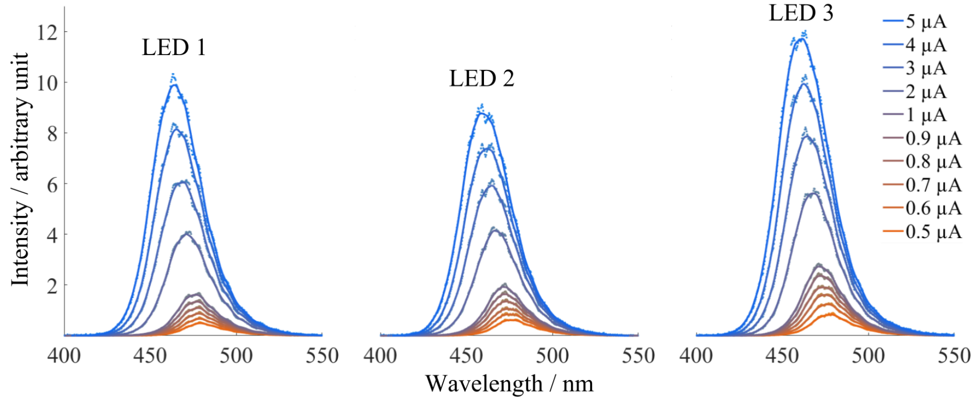

Figure 4.8: EL spectra from the first three single platelet LEDs featured in figure 4.1 for various DC levels. LEDs are spaced 2 µm apart and measured without moving the spectrometer fiber. The intensity is normalized for different integration times. Data points, also included in the plots, were smoothed by the MathWorks MATLAB *smooth* function with 20 points averaging span.

Table 4.1: Peak λ and FWHM values extracted from figure 4.8.

DC / µA	0.5	1	5
	Peak λ / nm		
LED 1	478.8	476.1	464.1
LED 2	475.8	471.5	458.8
LED 3	477.1	471.1	461.5
	FWHM / nm		
LED 1	24	26.3	34
LED 2	25.3	26.3	34.3
LED 3	25.3	27.3	35

The small values for FWHM at low currents is a good indication that most recombination is occurring inside the QW, close to the target $\lambda = 470$ nm, qualifying the LEDs for ChR2 activation. The blueshift for increasing current however, makes a good argument for using multiple QWs to counter the effects of well filling as charge carriers are being injected into the well at such a rate that they will more often recombine before reaching the band gap edge.

The lowest current noted to produce visible emission was 100 nA corresponding to around 3 V for the best rectifying single platelet diodes. This is similar to typical operation voltage levels for commercial blue LEDs. The partial optogenetic device light pattern in figure 4.9 shows how some platelets shine up like crazy bright diamonds while others do less so, indicating that R_S is different for individual diodes. Small variations in platelet p-GaN thickness and therefore also diode resistance would cause larger currents to take a certain path, also causing more contact annealing

on these platelets creating further disparity between diode current levels. A rather transient and flickering platelet light output, also points toward this conclusion. This first prototype idea was based on predictable light emission points spread out over a large area. The results suggest that a different approach is necessary to achieve optogenetic usefulness.

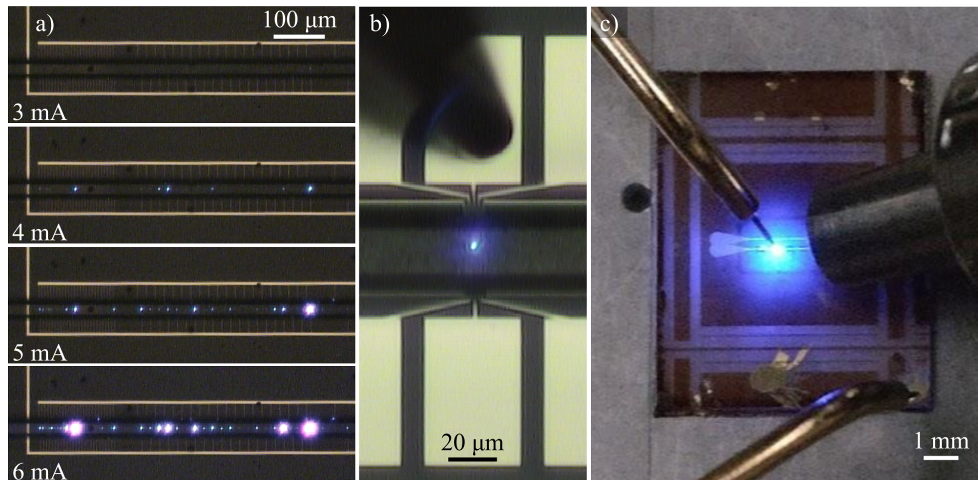

Figure 4.9: **a)** Microscope image of the bottom optogenetic row lighting up between 3 and 6 mA. The diode features bad I-V rectification. **b)** Rectifying single platelet emission with probe tip connected to the contact pad. **c)** Device chip with probes attached and spectrometer fiber brought in close for capturing the spectrum. Rectifying single platelet emission easily visible to the naked eye.

4.3 Biointegration

Despite the wire bond related issues other aspects of the biointegration and packaging were tested. The focus was centered on how well the passivation layer would work, which was experimentally tested by applying a voltage over a dummy sample, featuring every component but the LED chip, submerged in aCSF. The plan was to sweep the voltage and evaluate current leakage between pads through the conducting aCSF and how well the wire bonds and metal features had been insulated by the 40 nm Al_2O_3 film. However, measurements of leakage proved inconclusive and upon the voltage reaching ± 5 V, apparent precipitate would start to form over connected metal pads as shown in figure 4.10. These bubbles appear to originate near dark spots and close to the wire bond attachment point, hinting at a possible explanation being current leaking through Al_2O_3 defects or cracks. This phenomena warrants further investigation and should be addressed before the device is used with living cells.

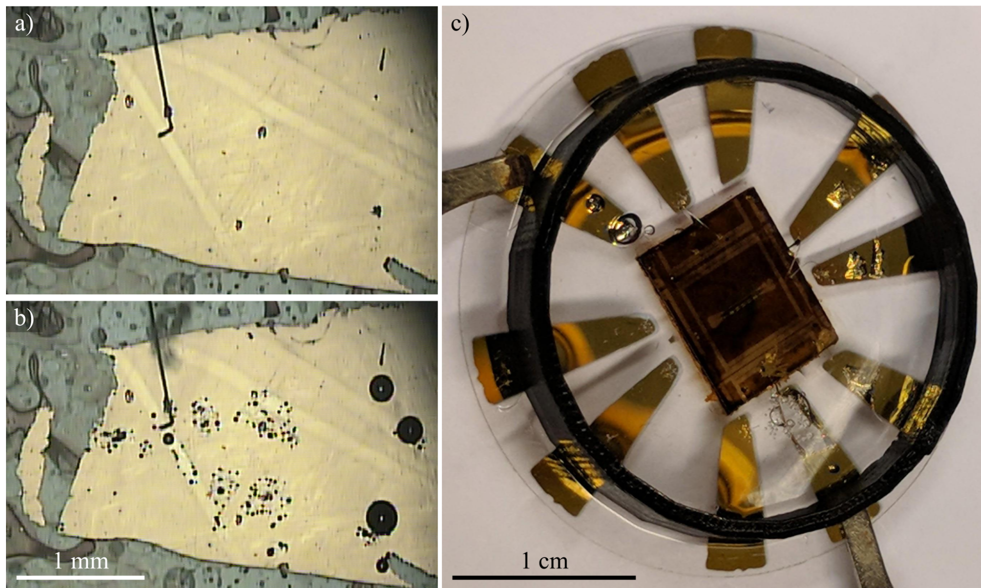

Figure 4.10: **a)** Dummy metal pad pre sweep **b)** Dummy pad post −5 to 5 V sweep. **c)** Final prototype with metal field lift-off after applying 5 V.

Similarly to the dummy sample, the final prototype was tested in the EEG lab with a Keithley 2400 SMU. In this experiment, part of the ground contact field detached when 5 V was applied which is also shown in figure 4.10. The observed effects could be caused by oxidation of the thin Ni layer while the damage further indicates that the passivation needs to be improved.

To end the chapter on a lighter note, primary neurons grown onto, unconnected, Al_2O_3 covered, sapphire based platelet LED chips, as part of the work of Daniel Jaghobi, are presented in figure 4.11. After some initial prohibitive issues with the cell incubator equipment, the use of poly-D-lysine and laminin adhesion coatings eventually proved successful in attaching neurons to the device chips.

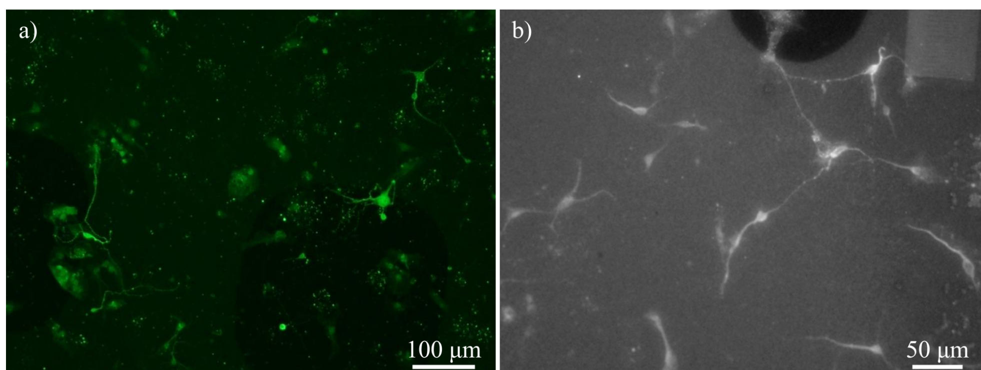

Figure 4.11: Fluoresence micrograpghs of primary neurons grown onto adhesion coated and passivated LED chips. Cells are stained for microtubule-associated protein 2 and neuronal nuclei markers with image **b)** having been converted to greyscale. Image courtesy of Daniel Jaghobi.

Chapter 5

Discussion

In this chapter, focus will be on the challenges faced and the goals we aimed for but did not reach, as well as suggesting improvements and explore some of the future perspectives and issues for µLEDs and optogenetics in a broader sense.

5.1 Prototype evaluation

While the ambitious goal of creating a high resolution optogenetic test platform was not fully realized, significant progress has been made on this path. Bright blue light emission and excellent electrical diode characteristics have been demonstrated for individual sub-micron GaN platelets. However, to develop the prototype into a functioning optogenetic instrument, a few hurdles remain to overcome or circumvent.

Regarding the ALD passivation, the rather obvious next thing to attempt would be using a significantly thicker Al_2O_3 film. Steude *et al.* have used a 1.3 µm thick Al_2O_3 compound encapsulation to protect their sensitve OLEDs for similar optogenetic purposes to good effect [7]. This may be a worthwhile change to the design without worsening the resolution notably, from the longer LED to cell separation. In addition to reducing permeation and current leakage I believe the potentially adverse effects of larger electric fields and high local temperatures could be mitigated. This should facilitate a safer environment for neurons and the ion rich aCSF solution. Furthermore, it is likely that a directed effort to clean the surfaces and keep them clean prior to passivation, is required. I am not certain the wire bonds will enjoy ultrasonic bath cleaning so the next thing to consider would be to reimagine the whole prototype packaging to simplify and remove unnecessary points of failure. For example, by increasing the device chip size to fit the entire pool rim on top, it could be integrated with a 3D printed custom made patch clamp rig adapter removing the need for wire bonds and the frail glass disc substrate altogether. EBL or UV lithography defined contact lines could be run under the rim and be made significantly thicker so they can be connected directly with crocodile clips to a current supply.

The difference in device series resistance can be solved by individually controlling the current supplied to each platelet and calls for an integrated solution with thin film transistor arrays for specifying which LEDs to light up. The chip p-side could then be bonded to the selection array die and have the sapphire substrate lift-off to create LEDs where light extraction chiefly occurs on the n-side. This would mean the p-side metal contact would serve as a light reflector. A device like the one described, would mean a huge improvement to the optogenetic usefulness of the device as any cell grown onto the array could be illuminated with good control over light intensity, which was also demonstrated by Stuede *et al.* [7]. A chemical mechanical polishing tool, for uniform flattening of whole platelet arrays or in between growth of semiconductor layers, may prove an useful addition to LNL and for the continued research on this topic [70].

For improving the device metallic contacts there are several options available. The use of a thermal contact annealing scheme could improve contact resistance, without having to run high current densities through individual diodes and a thinner evaporated Au layer for the actual platelet top contact would significantly increase light transmission. Incorporating indium tin oxide could also help to create an electrically viable and semitransparent p-side contact [71, 72] which is denoted by its frequent use in nitride LEDs [73–75]. Additionally, inductively coupled plasma RIE could be utilized to excavate through the Al_2O_3 and Si_3N_4 layers and provide a more controlled method than mechanical scratching to create the cathode [46]. A Ti/Al bilayer could also be introduced in order to reduce n-contact resistance [76].

Although the diodes were not optimally processed for maximum light extraction and efficiency, they did exhibit impressive visible emission for relatively low current levels. Integrating sphere analysis would therefore be very interesting for future devices to accurately establish the EQE. In regard to the single platelet vs parallel diode results I think the effort will prove its worth and provide a better understanding of the challenges the technology is facing as well as a basis to deal with them.

5.2 Future prospects

For the nitride platelet technology, two main development directions currently exist. First there is the efforts resulting in the spin-off company Hexagem, aiming to produce dislocation free GaN [77]. Second is the direction more related to this work, namely the development of micrometer sized, nitride light emitters in the entire visual and UV range promising more efficient, human centric and phosphor free white general lighting using red, green and blue (RGB) color mixing LEDs [46, 78].

Some other examples of applications include miniaturized, near infrared, vertical-cavity surface-emitting laser diodes, based on GaN platelets, that could be used for power efficient and fast optical interconnects in integrated circuits [79]. There is also the prospect of AlGaN

platelet LEDs accelerating the realization of UV water purification [80] and more optimized color mixing, solid state lighting for horticultural use, as it is proving increasingly practical [81] when efficiency is improved and costs are reduced.

The most obvious area of use for µLEDs though, is probably the digital display industry where the micrometer scale pitch distance between emitters would facilitate extremely high resolution devices especially attractive for virtual and augmented reality, wearable consumer electronics. The backlight free approach would additionally offer a great improvement over conventional liquid crystal display technology in terms of reduced power consumption and complexity as only used pixel elements would need to be lit up, facilitating longer battery endurance of mobile devices and thinner, more flexible displays in general. Already widely commercialized with OLED display systems, direct emitting subpixels have also proved their worth to enthusiasts of image quality as greatly improved black and bright contrasts can be achieved [82]. However, concerns about emitter lifetimes, burn-in effects and outdoor visibility [83] make a good case for transitioning to more robust inorganic LEDs.

Samsung, among others, are currently investing heavily into smaller LEDs for displays and recently unveiled a 146 ” unit dubbed *The Wall*, consisting of multiple modular µLED bricks [84]. The economic challenges facing the introduction to markets are still significant as legacy crystal and even the much newer OLED products are both mature and cost effective, but one has to appreciate the improvement and the simplicity offered by the inorganic µLED alternatives. Figure 5.1 showcases a speculative concept display based on epitaxially grown RGB platelet LEDs.

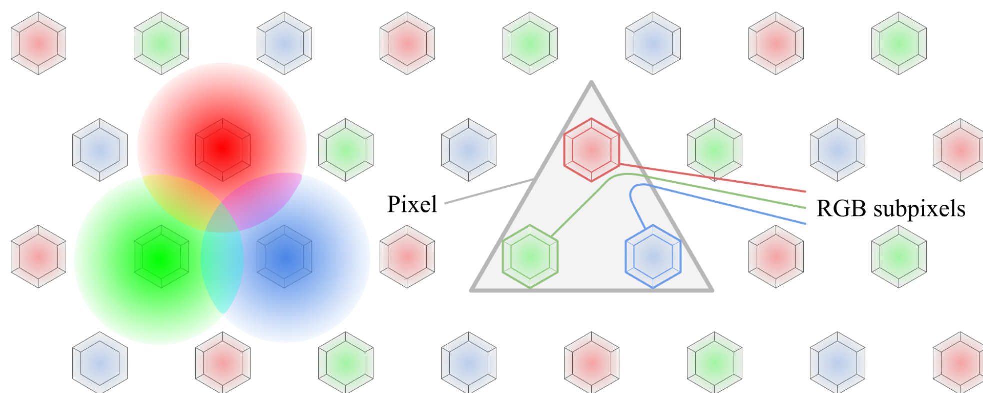

Figure 5.1: Grown separately, but on the same substrate, RGB GaN/InGaN subpixel, platelet LEDs, integrated to form a display element.

As for the future of optogenetics, I believe we have only seen the beginning of a field that will help us fill the crippling empty spaces in our understanding of the brain. The toolbox is expanding with a plethora of usable opsin membrane protein combinations, in addition to just ChR2, working at shifted wavelengths, to activate or inhibit

action potentials pulses [85]. Creative light injection methods for *in vivo* studies are being published on a regular basis, addressing the use of everything from fiber-optic waveguide optrodes [86] to photon frequency upconverting nanoparticles [87]. Another recent approach, technically not optogenetics but definitively in the same ballpark, is using laser illumination and photoinduced currents in cell culture integrated Si NWs to achieve localized neuron control but without the need for genetic modifications to the cells [88].

Further broadening our perspective on the use of light in medicine, we find examples of research that has met stringent patient safety criteria and led to actual therapeutic practice, in treatment of skin tumours with 630 nm laser emission [89]. The implications of a safe, light based method to treat cancer can not be overstated. Even if the extent to which it can cure the extremely complex and devastating group of diseases is minor today, maybe one of these days we will see, smart µLED implants making an appearance on this stage to help change that.

5.3 Ethics, risks and sustainability

It should be emphasized that the primary cell cultures used for the project were taken from put to death mice. It is opinioned by many, including myself, that this practice should be used restrictively and only when motivated by absolute necessity in furthering our understanding of science and medicine.

A critical question to ask before we start using optogenetics to treat neurological diseases in humans is whether we should control brain impulses and by extension thoughts and feelings, at all. Do the benefits of curing a disease this way weigh up for the risks with potential implants being hijacked? Could the technology be abused for brain engineering or as a subtle but devastating psychological weapon? This is of course highly speculative and assuming all obstacles with genetically modifying live person neurons and implants are overcome. Perhaps we will not need to worry about such things if optogentic fruition is preceded by viable cures from slow paced evolutionary medicine or other revolutionary breakthroughs, but I find the question an important one nonetheless.

LED energy savings in the United States have been predicted to cut the fraction of electricity use for lighting, from 20 % to 10 % by 2020 [90], but with these improvements in the availability of cheap light, the issue of induced demand should be considered [91]. To illustrate the point, imagine a stretch of, sparsely trafficked rural highway being illuminated by cheap, LED lamps as cost reductions allow for it without increasing the budget and the unnecessary adverse effects it may have on wildlife and light pollution. Inefficient industrial efforts to procure materials and fabricate the LED could waste some of the environmental gains and negate the reduced greenhouse gas emissions of powering a more efficient light source. There is also the question of how well we humans are adapting

to a world, increasingly lit up with sharp peak, bright LED light from displays and white light sources with at least one study suggesting the circadian rhythm can be altered and cognition performance negatively affected after evening exposure to a LED backlit computer screen [92]. The call for smart RGB color mixing LEDs that more truthfully emulate the natural sunlight spectra has merit and hopefully these can make LEDs even safer for us to view so we can keep enjoying their fantastic benefits.

Chapter 6

Conclusion

This report has covered the fabrication and characterization of nanostructure-based, blue, µLEDs as well as an experimental attempt to biointegrate and package these for *in vitro* optogenetic studies. Although the original aims of creating a prototype, high resolution optogenetic tool ultimately were not realized, important progress has been made toward this goal nonetheless. Bright blue LEDs with favorable I-V characteristics have been created and their quirks were studied. An empirical method for improving device performance with current induced, contact annealing has been proposed and a correlation between epitaxy and process inhomogeneity to the likelihood of diode rectification breakdown was observed. The findings presented in this thesis will be of use for future work within the nitride group to refine the platelet technique and device processing. As for the packaging and prototype design aspects of the project, many lessons were learned and experiences garnered, surely brightening the prospects for future combined effort projects aiming to create high resolution optogenetic platforms. Regardless of if my work is continued upon, it has been a true joy to participate in this project and I am confident we will only hear more of these amazing technologies, in years to come.

Acknowledgments

Although this report has been an individual endeavour, the project as a whole was nothing of the sort. I owe a great deal of gratitude to the following people who have supported me in many ways and enabled this work to be completed.

First and foremost I want to thank Olof for not just being the best supervisor to me conceivable, but also for enduring my learning curve and always taking the time to help. Continuing I want to thank Daniel, for introducing me to this opportunity and his positive attitude, even when faced with difficulties and Jenny for teaching me about optogenetics and her master's thesis work which laid the foundation for our interfaculty collaboration [93].

Thank you Mérab, Kristian Storm and Lars Samuelsson for developing the main project idea as well as Jonas and Mikael for the exciting platelet technique. I want to thank everyone else in the nitride group but especially Maryam, Bi and Taiping for their absolutely crucial and extraordinary epitaxy work and Ali Nowzari for the characterization advice. To Jovana Colvin I am grateful for her platelet scanning probe experiments and the ensuing morale boost. The EEG should not be forgotten for the much needed feedback and Esbjörn Melin specifically, who unknowingly greatly contributed to my report by having his master's thesis structure serve as a template and inspiration for mine [94].

I want to thank my examiner, Carina Fasth for the time she puts in for me to be able to do this project as a part of my education and together with Dan Hessman for the great course in semiconductor physics, without which I would probably have been stuck doing my diploma project over at the Department of Electrical and Information Technology. Christelle Prinz is acknowledged for her enthusiastic support on a wide range of bio-related inquires. Thank you Reine Wallenberg for the opportunity to present our project to a real life Nobel laureate and thank you Jacques Dubochet for showing genuine interest, even in a stressful time of being paraded around the country.

The next wave of thanks should go out to LNL and the Division of Solid State Physics staff members Ivan, George, Dmitry, Anders, David, Sara, Peter, Johanna and Abdul-Rehman for helping me with everything from risk assessments, tool training, computer software and room access. My office sharing colleagues Felix, Emil, Marcus, Robin and Oskar for the company and the ludicrously frequent walks. All my classmates who

have helped me get to this point and especially Azal who initially was slated to do this project but instead let me have a go at it for which I am very grateful.

Thanks to Hilbert Café for the delicious ciabattas all those days I did not have a food plan and the F-guild for enriching my time in Lund, for a brief while, truly making me feel like the coolest person in the world. Thank you Pink Floyd for the fantastic music and the inspiration throughout this thesis work and my life. I really do believe "We don't need no education" [95], but rather more of it.

I want to thank my family and closest friends for sticking around. I doubt I have deserved to be so lucky. And finally, thank you Fanny for the immense, unconditional love one simply should not be able to find but somehow stumbles into anyway. I dare not think of what would be of me if I had never met you.

References

1. Poher, V. *et al.* Micro-LED arrays: a tool for two-dimensional neuron stimulation. *Journal of Physics D: Applied Physics* **41,** 094014 (2008).
2. Cao, H., Gu, L., Mohanty, S. & Chiao, J. C. An integrated µLED optrode for optogenetic stimulation and electrical recording. *IEEE Transactions on Biomedical Engineering* **60,** 225–229 (2013).
3. Kim, T. I. *et al.* Injectable, cellular-scale optoelectronics with applications for wireless optogenetics. *Science* **340,** 211–216 (2013).
4. Kwon, K. & Li, W. *Integrated multi-LED array with three-dimensional polymer waveguide for optogenetics* in *2013 IEEE 26th International Conference on Micro Electro Mechanical Systems (MEMS)* (2013), 1017–1020.
5. Wu, F. *et al.* Monolithically integrated µLEDs on silicon neural probes for high-resolution optogenetic studies in behaving animals. *Neuron* **88,** 1136–1148 (2015).
6. Ayub, S. *et al. High-density probe with integrated thin-film micro light emitting diodes (µLEDs) for optogenetic applications* in *2016 IEEE 29th International Conference on Micro Electro Mechanical Systems (MEMS)* (2016), 379–382.
7. Steude, A., Witts, E. C., Miles, G. B. & Gather, M. C. Arrays of microscopic organic LEDs for high-resolution optogenetics. *Science Advances* **2,** e1600061 (2016).

8. Kim, K. *et al.* *GaN-on-Si μLED optoelectrodes for high-spatiotemporal-accuracy optogenetics in freely behaving animals* in *2016 IEEE International Electron Devices Meeting (IEDM)* (2016), 26.5.1–26.5.4.
9. Nakamura, S. Current Status of GaN-Based Solid-State Lighting. *MRS Bulletin* **34,** 101–107 (2009).
10. Tsao, J. Y. *et al.* Solid-state lighting: An energy-economics perspective. *Journal of Physics D: Applied Physics* **43,** 354001 (2010).
11. Haitz, R. & Tsao, J. Y. Solid-state lighting: 'The case' 10 years after and future prospects. *physica status solidi (a)* **208,** 17–29 (2011).
12. Shockley, W. The Theory of p-n Junctions in Semiconductors and p-n Junction Transistors. *Bell System Technical Journal* **28,** 435–489 (1949).
13. Schubert, E. F. *Light-Emitting Diodes* Second (Cambridge University Press, 2006).
14. Amano, H., Sawaki, N., Akasaki, I. & Toyoda, Y. Metalorganic vapor phase epitaxial growth of a high quality GaN film using an AlN buffer layer. *Applied Physics Letters* **48,** 353–355 (1986).
15. Amano, H. *et al.* Electron beam effects on blue luminescence of zinc-doped GaN. *Journal of Luminescence* **40-41,** 121–122 (1988).
16. Amano, H., Kito, M., Hiramatsu, K. & Akasaki, I. P-Type Conduction in Mg-Doped GaN Treated with Low-Energy Electron Beam Irradiation (LEEBI). *Japanese Journal of Applied Physics* **28,** L2112 (1989).
17. Nakamura, S., Mukai, T., Senoh, M. & Iwasa, N. Thermal Annealing Effects on P-Type Mg-Doped GaN Films. *Japanese Journal of Applied Physics* **31,** L139 (1992).
18. Nakamura, S., Iwasa, N., Senoh, M. & Mukai, T. Hole Compensation Mechanism of P-Type GaN Films. *Japanese Journal of Applied Physics* **31,** 1258 (1992).
19. Nakamura, S., Senoh, M. & Mukai, T. P-GaN/N-InGaN/N-GaN Double-Heterostructure Blue-Light-Emitting Diodes. *Japanese Journal of Applied Physics* **32,** L8 (1993).
20. Nakamura, S., Mukai, T. & Senoh, M. Candela-class high-brightness InGaN/AlGaN double-heterostructure blue-light-emitting diodes. *Applied Physics Letters* **64,** 1687–1689 (1994).
21. Narukawa, Y. *et al.* White light emitting diodes with super-high luminous efficacy. *Journal of Physics D: Applied Physics* **43,** 354002 (2010).
22. Sheu, J. K. *et al.* White-light emission from near UV InGaN-GaN LED chip precoated with blue/green/red phosphors. *IEEE Photonics Technology Letters* **15,** 18–20 (2003).

23. Hirayama, H. *et al. Realization of over 10% EQE AlGaN deep-UV LED by using transparent p-AlGaN contact layer* in *2016 International Semiconductor Laser Conference (ISLC)* (2016), 1–2.

24. Shih, H. Y. *et al.* Ultralow threading dislocation density in GaN epilayer on near-strain-free GaN compliant buffer layer and its applications in hetero-epitaxial LEDs. *Scientific Reports* **5,** 13671 (2015).

25. Porowski, S. Near defect free GaN substrates. *Materials Research Society Internet Journal of Nitride Semiconductor Research* **4,** 27–37 (1999).

26. Wang, W. *et al.* A new approach to epitaxially grow high-quality GaN films on Si substrates: the combination of MBE and PLD. *Scientific Reports* **6,** 24448 (2016).

27. Levinshtein, M., Rumyantsev, S. & Shur, M. *Properties of Advanced Semiconductor Materials: GaN, AIN, InN, BN, SiC, SiGe* (John Wiley & Sons, 2001).

28. Rinke, P. *et al.* Band gap and band parameters of InN and GaN from quasiparticle energy calculations based on exact-exchange density-functional theory. *Applied Physics Letters* **89,** 2004–2007 (2006).

29. Sze, S. M. & Lee, M. K. *Semiconductor Devices: Physics and Technology* Third (John Wiley & Sons, 2012).

30. Perevalov, T. V. *et al.* Electronic structure of α-Al_2O_3: Ab initio simulations and comparison with experiment. *JETP Letters* **85,** 165–168 (2007).

31. Santos, R. *et al.* Elucidating the high-k insulator α-Al_2O_3 direct/indirect energy band gap type through density functional theory computations. *Chemical Physics Letters* **637,** 172–176 (2015).

32. Liu, S. & Luo, X. *LED Packaging for Lighting Applications: Design, Manufacturing and Testing* (Wiley, 2011).

33. Takeuchi, T. *et al.* Quantum-Confined Stark Effect due to Piezoelectric Fields in GaInN Strained Quantum Wells. *Japanese Journal of Applied Physics* **36,** L382 (1997).

34. Ju, Z. *et al.* On the origin of the redshift in the emission wavelength of InGaN/GaN blue light emitting diodes grown with a higher temperature interlayer. *Applied Physics Letters* **100,** 123503 (2012).

35. Stringfellow, G. Microstructures produced during the epitaxial growth of InGaN alloys. *Journal of Crystal Growth* **312,** 735–749 (2010).

36. Iveland, J. *et al.* Direct Measurement of Auger Electrons Emitted from a Semiconductor Light-Emitting Diode under Electrical Injection: Identification of the Dominant Mechanism for Efficiency Droop. *Physical Review Letters* **110,** 177406 (2013).

37. Ohlsson, J. & Björk, M. US 9653286 B2 (2017).

38. Qian, F. *et al.* Core/Multishell Nanowire Heterostructures as Multicolor, High-Efficiency Light-Emitting Diodes. *Nano Letters* **5,** 2287–2291 (2005).

39. Bavencove, A. L. *et al.* Light emitting diodes based on GaN core/shell wires grown by MOVPE on n-type Si substrate. *Electronics Letters* **47,** 765–767 (2011).

40. Koester, R. *et al.* M-Plane Core–Shell InGaN/GaN Multiple-Quantum-Wells on GaN Wires for Electroluminescent Devices. *Nano Letters* **11,** 4839–4845 (2011).

41. Guan, N. *et al.* Flexible White Light Emitting Diodes Based on Nitride Nanowires and Nanophosphors. *ACS Photonics* **3,** 597–603 (2016).

42. Rishinaramangalam, A. K. *et al.* Semipolar InGaN/GaN nanostructure light-emitting diodes on c -plane sapphire. *Applied Physics Express* **9,** 032101 (2016).

43. Humphreys, C. *et al.* The atomic structure of polar and non-polar InGaN quantum wells and the green gap problem. *Ultramicroscopy* **176,** 93–98 (2017).

44. Kishino, K. & Ishizawa, S. Selective-area growth of GaN nanocolumns on Si(111) substrates for application to nanocolumn emitters with systematic analysis of dislocation filtering effect of nanocolumns. *Nanotechnology* **26,** 225602 (2015).

45. Choi, K., Arita, M. & Arakawa, Y. Selective-area growth of thin GaN nanowires by MOCVD. *Journal of Crystal Growth* **357,** 58–61 (2012).

46. Monemar, B., Ohlsson, B. J., Gardner, N. F. & Samuelson, L. in *Semiconductor Nanowires II: Properties and Applications* (eds Dayeh, S. A., i Morral, A. F. & Jagadish, C.) 227–271 (Elsevier, 2016).

47. Deisseroth, K. Optogenetics. *Nature Methods* **8,** 26–29 (2011).

48. Boyden, E. S. *et al.* Millisecond-timescale, genetically targeted optical control of neural activity. *Nature Neuroscience* **8,** 1263–1268 (2005).

49. Zhang, F., Wang, L. P., Boyden, E. S. & Deisseroth, K. Channelrhodopsin-2 and optical control of excitable cells. *Nature Methods* **3,** 785–792 (2006).

50. Foutz, T. J., Arlow, R. L. & McIntyre, C. C. Theoretical principles underlying optical stimulation of a channelrhodopsin-2 positive pyramidal neuron. *Journal of Neurophysiology* **107,** 3235–3245 (2012).

51. Stark, E., Koos, T. & Buzsáki, G. Diode probes for spatiotemporal optical control of multiple neurons in freely moving animals. *Journal of Neurophysiology* **108,** 349–363 (2012).

52. Azevedo, F. A. *et al.* Equal numbers of neuronal and nonneuronal cells make the human brain an isometrically scaled-up primate brain. *The Journal of Comparative Neurology* **513,** 532–541 (2009).

53. Alberts, B. *et al. Essential Cell Biology* Fourth (Garland Science, 2014).

54. Fisher, R. S. *et al.* ILAE Official Report: A practical clinical definition of epilepsy. *Epilepsia* **55,** 475–482 (2014).

55. Fisher, R. S. *et al.* Epileptic Seizures and Epilepsy: Definitions Proposed by the International League Against Epilepsy (ILAE) and the International Bureau for Epilepsy (IBE). *Epilepsia* **46,** 470–472 (2005).

56. Vos, T. *et al.* Global, regional, and national incidence, prevalence, and years lived with disability for 310 diseases and injuries, 1990–2015: a systematic analysis for the Global Burden of Disease Study 2015. *The Lancet* **388,** 1545–1602 (2016).

57. Wang, H. *et al.* Global, regional, and national life expectancy, all-cause mortality, and cause-specific mortality for 249 causes of death, 1980–2015: a systematic analysis for the Global Burden of Disease Study 2015. *The Lancet* **388,** 1459–1544 (2016).

58. Eadie, M. J. Shortcomings in the current treatment of epilepsy. *Expert review of Neurotherapeutics* **12,** 1419–1427 (2012).

59. Tønnesen, J. *et al.* Optogenetic control of epileptiform activity. *Proceedings of the National Academy of Sciences of the United States of America* **106,** 12162–12167 (2009).

60. Malmivuo, J. & Plonsey, R. *Bioelectromagnetism: Principles and Applications of Bioelectric and Biomagnetic Fields* 66–105 (Oxford University Press, 1995).

61. Stoffel, A., Kovács, A., Kronast, W. & Müller, B. LPCVD against PECVD for micromechanical applications. *Journal of Micromechanics and Microengineering* **6,** 1 (1996).

62. Hultin, O. *Nanostructures for Optoelectronics: Device Fabrication and Characterization* PhD thesis (Lund University, 2018).

63. Zhang, L. *et al.* Annealing of Al_2O_3 thin films prepared by atomic layer deposition. *Journal of Physics D: Applied Physics* **40,** 3707 (2007).

64. *MICROPOSIT^{TM} S1800^{TM} G2 SERIES PHOTORESISTS For Microlithography Applications* 889-00032. Rev. 0. The Dow Chemical Company (2014). `http://microchem.com/PDFs_Dow/S1800-G2.pdf` (2018-03-22).

65. *NANO^{TM} PMMA and Copolymer* MicroChem Corp. (2001). `http://www.microchem.com/pdf/PMMA_Data_Sheet.pdf` (2018-03-27).

66. Sheu, J. K. *et al.* High-transparency Ni/Au ohmic contact to p-type GaN. *Applied Physics Letters* **74,** 2340–2342 (1999).

67. Klumbies, H. *et al.* Thickness dependent barrier performance of permeation barriers made from atomic layer deposited alumina for organic devices. *Organic Electronics: physics, materials, applications* **17,** 138–143 (2015).

68. Finch, D. S. *et al.* Biocompatibility of atomic layer-deposited alumina thin films. *Journal of Biomedical Materials Research Part A* **87A,** 100–106 (2007).

69. Kolodzey, J. *et al.* Electrical conduction and dielectric breakdown in aluminum oxide insulators on silicon. *IEEE Transactions on Electron Devices* **47,** 121–128 (2000).

70. Porowski, S. Bulk and homoepitaxial GaN-growth and characterisation. *Journal of Crystal Growth* **189-190,** 153–158 (1998).

71. Horng, R.-H., Wuu, D. S., Lien, Y. C. & Lan, W. H. Low-resistance and high-transparency Ni/indium tin oxide ohmic contacts to p-type GaN. *Applied Physics Letters* **79,** 2925–2927 (2001).

72. Kim, S. Y., Jang, H. W. & Lee, J. L. Transparent Ohmic Contacts on p-GaN Using an Indium Tin Oxide Overlayer. *physica status solidi (c)* **0,** 214–218 (2002).

73. Kim, S. Y., Jang, H. W. & Lee, J. L. High-brightness GaN-based light-emitting diode with indium tin oxide based transparent ohmic contact. *Journal of Vacuum Science & Technology B: Microelectronics and Nanometer Structures Processing, Measurement, and Phenomena* **22,** 1851–1857 (2004).

74. Liu, Y. J. *et al.* Implementation of an indium-tin-oxide (ITO) direct-Ohmic contact structure on a GaN-based light emitting diode. *Optics Express* **19,** 14662–14670 (2011).

75. Jiang, Y. *et al.* Realization of high-luminous-efficiency InGaN light-emitting diodes in the "green gap" range. *Scientific Reports* **5,** 10883 (2015).

76. Lin, M. *et al.* Low resistance ohmic contacts on wide band-gap GaN. *Applied Physics Letters* **64,** 1003–1005 (1994).

77. Hexagem company webpage. `http://www.hexagem.se` (2018-04-27).

78. Yang, G. *et al.* InGaN/GaN multiple quantum wells on selectively grown GaN microfacets and the applications for phosphor-free white light-emitting diodes. *Reviews in Physics* **1,** 101–119 (2016).

79. Szczerba, K. *et al.* 4-PAM for high-speed short-range optical communications. *IEEE/OSA Journal of Optical Communications and Networking* **4,** 885–894 (2012).

80. Banas, M. A. *et al.* *Final LDRD Report: Ultraviolet Water Purification Systems for Rural Environments and Mobile Applications* tech. rep. SAND2005-7245 (Sandia National Laboratories, 2005).
81. Morrow, R. C. LED lighting in horticulture. *HortScience* **43,** 1947–1950 (2008).
82. Kunić, S. & Šego, Z. *OLED technology and displays* in *Proceedings ELMAR-2012* (2012), 31–35.
83. Laaperi, A. OLED lifetime issues from a mobile-phone-industry point of view. *Journal of the Society for Information Display* **16,** 1125–1130 (2012).
84. Samsung "The Wall" unveil. `https://news.samsung.com/global/samsung-unveils-the-wall-the-worlds-first-modular-microled-146-inch-tv` (2018-04-27).
85. Deisseroth, K. Optogenetics: 10 years of microbial opsins in neuroscience. *Nature Neuroscience* **18,** 1213–1225 (2015).
86. Aravanis, A. M. *et al.* An optical neural interface: in vivo control of rodent motor cortex with integrated fiberoptic and optogenetic technology. *Journal of neural engineering* **4,** S143 (2007).
87. Chen, S. *et al.* Near-infrared deep brain stimulation via upconversion nanoparticle–mediated optogenetics. *Science* **359,** 679–684 (2018).
88. Parameswaran, R. *et al.* Photoelectrochemical modulation of neuronal activity with free-standing coaxial silicon nanowires. *Nature Nanotechnology* **13,** 260–266 (2018).
89. Svanberg, K. *et al.* Photodynamic therapy of non-melanoma malignant tumours of the skin using topical δ-amino levulinic acid sensitization and laser irradiation. *British Journal of Dermatology* **130,** 743–751 (1994).
90. Bergh, A., Craford, G., Duggal, A. & Haitz, R. The promise and challenge of solid-state lighting. *Physics today* **54,** 42–47 (2001).
91. Schubert, E. F. & Kim, J. K. Solid-State Light Sources Getting Smart. *Science* **308,** 1274–1278 (2005).
92. Cajochen, C. *et al.* Evening exposure to a light-emitting diodes (LED)-backlit computer screen affects circadian physiology and cognitive performance. *Journal of Applied Physiology* **110,** 1432–1438 (2011).
93. Wickham, J. *Optogenetic Activation of Hippocampal Neurons with Nanowire Light Emitting Diode: Development of a Nanowire Light Emitting Diode Probe* MA thesis (Lund University, 2013).
94. Melin, E. *Optogenetic kindling* MA thesis (Lund University, 2013).
95. Waters, R. *Another Brick in the Wall (Part 2)* Harvest Records. 1979.